Published OnlineFirst June 24, 2014; DOI: 10.1158/1078-0432.CCR-14-0072

Clinical Cancer Research

Reversible LSD1 Inhibition Interferes with Global EWS/ETS Transcriptional Activity and Impedes Ewing Sarcoma Tumor Growth

Savita Sankar, Emily R. Theisen, Jared Bearss, et al.

Clin Cancer Res 2014;20:4584-4597. Published OnlineFirst June 24, 2014.

Published OnlineFirst June 24, 2014; DOI: 10.1158/1078-0432.CCR-14-0072

Cancer Therapy: Preclinical

Clinical Cancer Research

Reversible LSD1 Inhibition Interferes with Global EWS/ETS Transcriptional Activity and Impedes Ewing Sarcoma Tumor Growth

Savita Sankar[1], Emily R. Theisen[2,3], Jared Bearss[2], Timothy Mulvihill[4], Laura M. Hoffman[5], Venkataswamy Sorna[2], Mary C. Beckerle[1,5], Sunil Sharma[2,6], and Stephen L. Lessnick[1,7,8]

Abstract

Purpose: Ewing sarcoma is a pediatric bone tumor that absolutely relies on the transcriptional activity of the EWS/ETS family of fusion oncoproteins. While the most common fusion, EWS/FLI, utilizes lysine-specific demethylase 1 (LSD1) to repress critical tumor suppressors, small-molecule blockade of LSD1 has not yet been thoroughly explored as a therapeutic approach for Ewing sarcoma. We therefore evaluated the translational potential of potent and specific LSD1 inhibition with HCI2509 on the transcriptional program of both EWS/FLI and EWS/ERG as well as the downstream oncogenic phenotypes driven by EWS/ETS fusions in both *in vitro* and *in vivo* models of Ewing sarcoma.

Experimental Design: RNA-seq was used to compare the transcriptional profiles of EWS/FLI, EWS/ERG, and treatment with HCI2509 in both EWS/FLI- and EWS/ERG-containing cell lines. We then evaluated morphologic phenotypes of treated cells with immunofluorescence. The induction of apoptosis was evaluated using caspase-3/7 activation and TUNEL staining. Colony forming assays were used to test oncogenic transformation and xenograft studies with patient-derived cell lines were used to evaluate the effects of HCI2509 on tumorigenesis.

Results: HCI2509 caused a dramatic reversal of both the up- and downregulated transcriptional profiles of EWS/FLI and EWS/ERG accompanied by the induction of apoptosis and disruption of morphologic and oncogenic phenotypes modulated by EWS/FLI. Importantly, HCI2509 displayed single-agent efficacy in multiple xenograft models.

Conclusions: These data support epigenetic modulation with HCI2509 as a therapeutic strategy for Ewing sarcoma, and highlight a critical dual role for LSD1 in the oncogenic transcriptional activity of EWS/ETS proteins. *Clin Cancer Res; 20(17); 4584–97. ©2014 AACR.*

Introduction

Dynamic epigenetic regulation, including DNA methylation and posttranslational histone modification, is required for normal development and maintenance of tissue-specific transcriptional programs. Abnormal regulation can lead to altered gene expression and malignant transformation (1, 2). Indeed, enzymes which mediate epigenetic modifications are emerging as therapeutic targets in cancer (1, 2). Histone lysine methylation, specifically, can signify both activating and repressive chromatin, depending on the site of methylation (3). For example, methylation at histone H3K4 indicates active chromatin while methylation at H3K9 and H3K27 indicates repressive chromatin (3). While DNA methyltransferases (DNMT) and histone deacetylases (HDAC) are involved in global epigenetic processes, histone lysine methyltransferases (KMT) and demethylases (KDM) regulate histone methylation and gene expression in a manner that is often cell-type specific (4–8). Genetic mutations, chromosomal translocations, and translocation-derived fusion proteins affecting KMTs and KDMs contribute to impaired tumor suppression

[1]Department of Oncological Sciences, University of Utah School of Medicine, Salt Lake City, Utah. [2]Center for Investigational Therapeutics at Huntsman Cancer Institute, University of Utah, Salt Lake City, Utah. [3]Department of Pharmaceutics and Pharmaceutical Chemistry, College of Pharmacy, University of Utah, Salt Lake City, Utah. [4]University of Utah School of Medicine, Salt Lake City, Utah. [5]Department of Biology, Huntsman Cancer Institute, University of Utah, Salt Lake City, Utah. [6]Division of Medical Oncology, University of Utah School of Medicine, Salt Lake City, Utah. [7]Center for Children's Cancer Research at Huntsman Cancer Institute, Salt Lake City, Utah. [8]Division of Pediatric Hematology/Oncology, University of Utah School of Medicine, Salt Lake City, Utah.

Note: Supplementary data for this article are available at Clinical Cancer Research Online (http://clincancerres.aacrjournals.org/).

Savita Sankar and Emily R. Theisen contributed equally to this article.

Current address for S. Sankar: Massachusetts General Hospital Cancer Center and the Department of Medicine, Harvard Medical School, Boston, MA 02115.

Corresponding Author: Stephen L. Lessnick, Center for Children's Cancer Research, Huntsman Cancer Institute, 2000 Circle of Hope, Room 4242, Salt Lake City, UT 84112. Phone: 801-585-9268; Fax: 1-801-585-5357; E-mail: stephen.lessnick@hci.utah.edu

doi: 10.1158/1078-0432.CCR-14-0072

Published OnlineFirst June 24, 2014; DOI: 10.1158/1078-0432.CCR-14-0072

Translational Relevance

Ewing sarcoma is an aggressive cancer, with bleak survival rates (10%–30%) for patients with metastatic or relapsed disease. Treatment with the LSD1 inhibitor HCI2509 disrupts the global transcriptional function of EWS/ETS fusions, impairs multiple EWS/ETS-associated oncogenic phenotypes, and shows single-agent efficacy in multiple xenograft models of Ewing sarcoma. With several targeted LSD1 inhibitors in preclinical development, these results highlight a new therapeutic strategy for this disease.

and altered developmental plasticity in several malignancies (8–14). Strategies targeting individual KMTs and KDMs critical for a particular malignancy may confer increased therapeutic specificity (15).

Lysine-specific demethylase 1 (LSD1) is a KDM implicated in neuroblastoma, acute myeloid leukemia, breast, prostate, bladder, lung, liver, and colorectal tumors (16–21). Recently, high LSD1 expression was reported in certain mesenchymal tumors, including Ewing sarcoma (22, 23). Ewing sarcoma is a highly aggressive pediatric malignancy characterized by the presence of a translocation-derived fusion oncoprotein and aberrant transcription factor, EWS/FLI (24). The majority of cases present with the EWS/FLI fusion, while several other related EWS/ETS fusions are occasionally observed as well (25). The most common of these is EWS/ERG, which presents in approximately 10% of cases (25). While the 5-year overall survival for patients with local disease is 70% to 80%, for those who present with metastases, or those who have relapsed, this drops to a bleak 10% to 30% (26, 27). In addition, treatment carries elevated risk for long-term side effects, including limb dysfunction, infertility, and secondary malignancies (28). Targeted therapies with increased efficacy and reduced toxicity are imperative. Though the role of LSD1 in Ewing sarcoma pathogenesis was still vague, the LSD1 inhibitor tranylcypromine impaired growth of Ewing sarcoma cell lines *in vitro* (23). Tranylcypromine is used clinically as a monoamine oxidase inhibitor, but has low potency as an LSD1 inhibitor, and has several documented off-target effects precluding widespread clinical use targeting this enzyme.

Further investigation showed LSD1 recruitment by EWS/FLI as a member of the nucleosome remodeling and histone deacetylase (NuRD) complex to repress the critical EWS/FLI targets *LOX* and *TGFBR2* (29). Treatment with the potent LSD1 inhibitor, HCI2509, caused derepression of these genes and impaired tissue culture cell viability in multiple Ewing sarcoma cell lines at physiologically relevant concentrations (29). The sensitivity of multiple cell lines to LSD1 inhibition suggests a pivotal role for LSD1 in Ewing sarcoma beyond repression of select EWS/FLI targets. The extent of the role that LSD1 plays in the global transcriptional program orchestrated by EWS/FLI, and other EWS/ETS fusions, remains uncharacterized. The experiments herein describe the global transcriptional effects of HCI2509 treatment in Ewing sarcoma and the downstream antitumor effects that result.

Materials and Methods

Constructs and retroviruses

The Luciferase-RNAi (Luc-RNAi), EWS/FLI-RNAi (EF-2-RNAi), 3x-FLAG EWS/FLI, 3x-FLAG Δ22, and 1x-FLAG R2L2 cDNA are previously described (30–32). The 1x-HA HMOX1 cDNA was generated and subcloned into the Murine Stem Cell Virus (MSCV) retroviral vector (Clontech). siRNA controls targeted toward LSD1, CHD4, REST, RCoR1, NCoR, and Sin3A are described previously (29).

Antibodies and reagents

The following antibodies were used for immunodetection: M2-anti-FLAG (HRP; Sigma A8592), anti-FLI-1 (Santa-Cruz sc-356X), anti-α-Tubulin (Calbiochem CP06), anti-HA (Abcam ab9110), anti-H3 total (Abcam ab1791), anti-H3K4 me1 (Abcam ab8895), anti-H3K4 me2 (Millipore, 07–030), anti-H3K4 me3 (Active Motif, 39159), anti-H3K9 me1 (Abcam ab9045), anti-H3K9 me2 (Abcam ab1220), anti-H3K9 me3 (Abcam ab8898), anti-HMOX1 (Sigma SAB1410641), anti-Paxillin (BD Transduction Labs 610619), anti-LSD1 (Cell Signaling Technology 2184) AlexaFluor secondary (Molecular Probes), AlexaFluor Phalloidin (Molecular Probes). HCI2509 is previously described (33).

Cell culture

Ewing sarcoma cell lines harboring the EWS/FLI (A673, TC-71, SK-N-MC, SKES1, and EWS502) or EWS/ERG fusion (TTC-466) were grown in appropriate selection media, as previously described (34, 35). NIH 3T3 cells with and without EWS/FLI expression were previously reported (36). Growth assays (3T5) were previously described (35).

Colony formation assays

Soft agar assays were described previously (35). Methylcellulose assays were performed by plating 1×10^5 cells in a 1:1 mix of 2% methylcellulose and growth media as described previously (29).

Quantitative reverse-transcriptase PCR

Total RNA was extracted using an RNeasy kit (Qiagen). Total RNA was then amplified and detected using SYBR green fluorescence for quantitation. Normalized fold enrichment was calculated by determining the fold-change of each condition relative to the control. The data in each condition was normalized to internal housekeeping control genes, *GAPDH* and *RPL19*. Primer sequences are provided in Supplementary Data (Supplementary Table S3).

Chromatin immunoprecipitation

Chromatin immunoprecipitation (ChIP) was performed as previously described (37) using anti-LSD1 antibody (Abcam ab17721). Quantitative PCR was performed with *HMOX1* gene primers amplifying a region ~29 base pairs

Published OnlineFirst June 24, 2014; DOI: 10.1158/1078-0432.CCR-14-0072

upstream of the transcription start site (TSS). *BCL2L1* was used as a normalization control (38). Primer sequences are provided in the Supplementary Data (Supplementary Table S3).

In vivo studies

Xenografts: A673, SK-N-MC, or SKES1 cells were injected into the right hindflanks of nude mice at 1×10^6 cells or 1×10^6 cells or 2.5×10^6 cells per flank, respectively. For all xenograft studies, 10 mice per condition were injected subcutaneously; therefore, 10 tumors were measured per group. In the SK-N-MC study, one animal perished due to an unrelated rash and was censored from analysis. Tumors were measured using digital calipers and volumes were calculated as follows: $(L \times W \times D)/2$. Treatment was initiated on day 7 after bioluminescent imaging confirmed tumor engraftment in the A673 study, whereas SK-N-MC and SKES1 studies were initiated once tumors reached a volume of >100 mm^3. Mice in each group were sacrificed once tumors reached a size limit of 2 cm^3. Kaplan–Meier survival curves were plotted using GraphPad Prism. Tumor volume and body weight were recorded for all three models. Harvested tumors were flash frozen, homogenized by mortar and pestle in liquid nitrogen, and analyzed for RNA or protein. All xenograft experiments were performed in accordance with protocol 11–11003 approved by the University of Utah Institutional Animal Care and Use Committee.

Blood Counts: The facial vein was identified and pierced with a lancet, blood was collected in a heparin capillary tube, and analyzed using a HemaTrue hematology analyzer (Heska).

Immunofluorescence assays

A total of 5×10^4–1.5×10^5 A673 and TTC-466 cells were seeded onto fibronectin-coated coverslips, allowed to adhere for ≥24 hours, treated with vehicle or HCI2509 at 0.5, 1, and 2 μmol/L for 3 days in DMEMc + 10% FBS, and fixed, stained, and imaged as previously described (39). Briefly, cells were immunostained with paxillin antibody (1:100) or LSD1 antibody (1:400) and then with secondary antibody (1:100) and DAPI (0.3 μmol/L). Fluorescent cell images were collected on a Zeiss Axioskop2 mot plus microscope with a 40 × dry objective (NA 0.75 NeoFluor), Axiocam MR camera, and Axiovision v4.8.1 software (Carl Zeiss MicroImaging, Inc.). Cell area analysis was performed with ImageJ (NIH freeware) and MetaMorph software (Molecular Devices); ≥50 cells were analyzed from ≥10 microscope fields, conversion factor 1 μm = 6.2 pixels. Image datasets were analyzed in GraphPad Prism 5 using unpaired *t*-tests and graphed as mean and SD.

RNA sequencing analysis, GSEA, and Venn overlaps

See Supplementary Methods for a description of RNA-seq data collection. Overlaps between the different gene sets were performed using VennMaster (http://www.informatik.uni-ulm.de/ni/mitarbeiter/HKestler/vennm/doc.html). Statistical significance of the overlaps was determined using χ^2 analysis. Gene set enrichment analysis (GSEA) was performed using GSEA v2.0.10 (http://www.broad.mit.edu/gsea/). Functional annotation analysis was performed by DAVID (david.abcc.ncifcrf.gov). Heatmaps were generated by converting read counts to fragments per kilobase gene model per million reads (FPKM). Genes were included in the heatmap if their differential abundance was more than 3-fold in both experiments and the Benjamini–Hochberg false discovery rate was <0.05. The data were normalized per gene across both experiments and $\log_{10}$ transformed. Heatmaps were created using the R gplots package. Ranks were based on averages of treatment and control.

Cell viability determination and EC_{50} shift analysis

A673 cells were stably infected and selected for expression of control Luc-RNAi or EF-2-RNAi. A total of 2×10^4 cells per well were seeded in a 96-well plate, allowed 24 hours to adhere, and treated with either vehicle or HCI2509 for 96 hours. Viability was assayed using CellTiter-Glo (Promega).

In vitro apoptosis assays

Caspase/viability. 2×10^4 cells per well were seeded in a 96-well plate, treated with either vehicle or two times their respective EC_{50} for HCI2509. Caspase activation and cell viability were assayed using Caspase-Glo 3/7 (Promega) and CellTiter-Glo (Promega), respectively, at 0, 24, and 48 hours.

TUNEL staining. A673 cells were treated with either vehicle or 2 μmol/L HCI2509 for 48 hours and then assayed using the DeadEnd Colorimetric TUNEL (Promega). Images were collected on an Olympus 1 × 70 inverted microscope, Olympus EOS Rebel XSi camera, and EOS Utility software (Canon U.S.A., Inc.).

Data availability

Raw sequence reads can be found in the NCBI SRA under numbers SRA096343, SRA096347, SRA096354. Differentially expressed genes from each RNA-seq dataset are in Supplementary Table S1.

Results

LSD1 inhibition reverses the EWS/ETS-driven transcriptional program in Ewing sarcoma

HCI2509 is a specific and reversible noncompetitive inhibitor of LSD1 previously shown to derepress the critical EWS/FLI target genes *LOX* and *TGFBR2* and to kill multiple Ewing sarcoma cell lines *in vitro* (29, 30). Interestingly, HCI2509-mediated derepression of *LOX* and *TGFBR2* was dependent on the expression of EWS/FLI. To determine whether the Ewing sarcoma cell death observed with HCI2509 treatment was also dependent on EWS/FLI, we knocked down the fusion protein using retroviral-mediated shRNA, and assessed viability after treatment with HCI2509. Cells expressing EWS/FLI were approximately 10-fold more susceptible to treatment with HCI2509 compared to cells with EWS/FLI knockdown (Fig. 1A), which confirmed the efficacy of HCI2509 is dependent upon the presence of EWS/FLI. On the basis of previous results showing that HCI2509 decreased viability in multiple

Published OnlineFirst June 24, 2014; DOI: 10.1158/1078-0432.CCR-14-0072

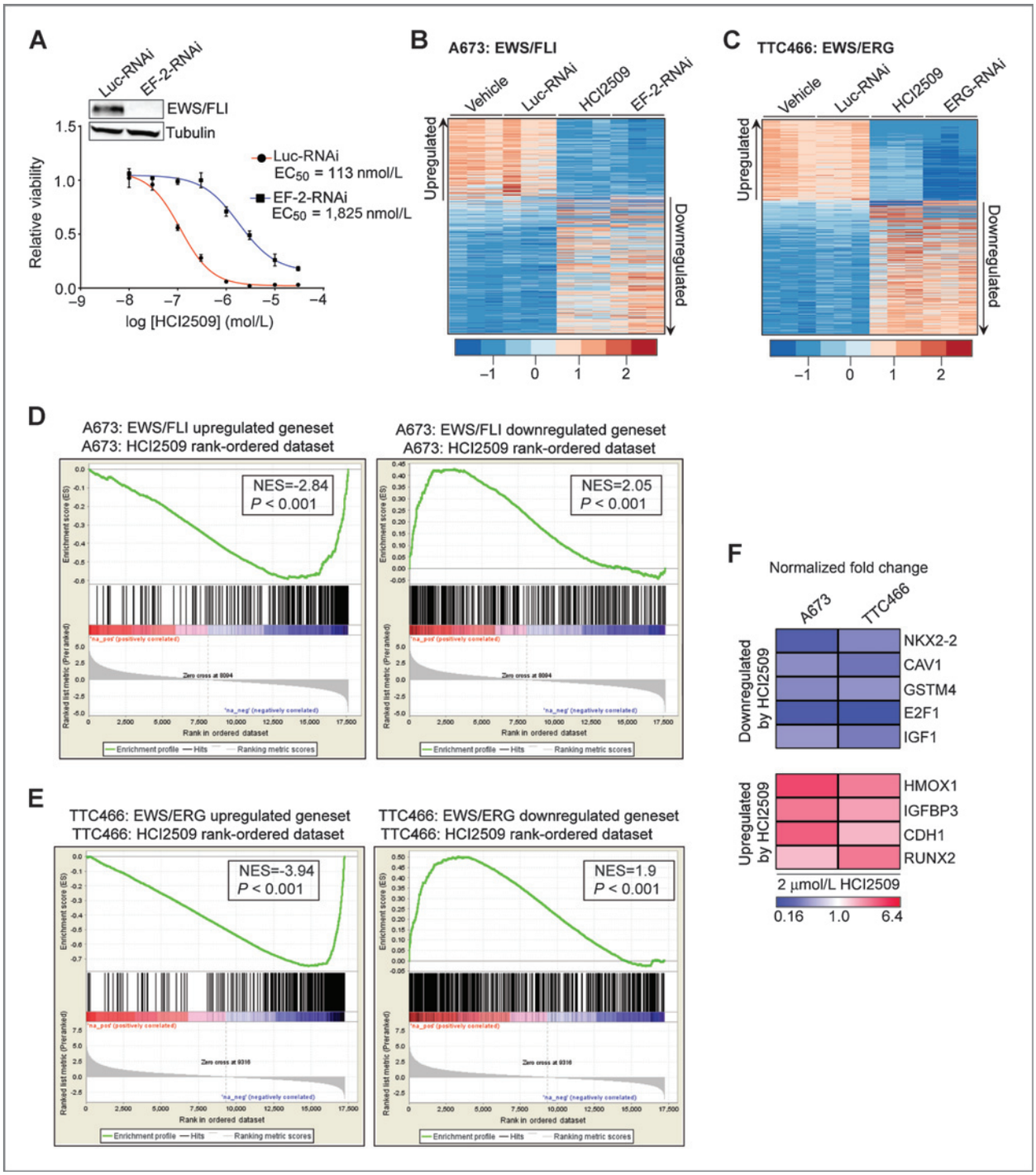

Figure 1. Global EWS/FLI transcriptional activity is disrupted by HCI2509. A, cell viability assay showing the difference in HCI2509 sensitivity between A673 cells with control [EC_{50} = 113 nmol/L; 95% confidence interval (CI), 81.9–158 nmol/L] and EWS/FLI knockdown (EC_{50} = 1,825 nmol/L; 95% CI, 1,111–2,999 nmol/L). The dose–response curves were determined after 96 hours of treatment and normalized to the vehicle controls. Mean and SD are shown ($n = 3$). Stable EWS/FLI knockdown was analyzed by Western Blot analysis as shown in the inset. B and C, heatmap representation of the HCI2509 expression profile matched to the rank-ordered EWS/FLI- (B) and EWS/ERG knockdown (C) profiles. Genes were ranked by mean deviation of the log-transformed FPKM (Fragments Per Kilobase per Million mapped reads). The columns for each condition represent one independent biologic replicate. Each row represents a different gene. D and E, GSEA from RNA-seq experiments using the EWS/FLI–regulated genes (D) in A673 cells as the rank-ordered dataset and the 281 HCI2509 upregulated and 376 HCI2509 downregulated genes as the gene sets and EWS/ERG–regulated genes (E) in TTC-466 cells as the rank-ordered dataset and the 216 HCI2509 upregulated and 357 HCI2509 downregulated genes as the gene sets. Normalized enrichment scores (NES) and *P* values are shown. F, qRT-PCR validation of *NKX2.2*, *CAV1*, *GSTM4*, *E2F1*, *IGF-1*, *RUNX2*, *IGFBP3*, *HMOX1*, and *CDH1* as HCI2509 targets in A673 and TTC-466 cells treated for 48 hours with vehicle or HCI2509 at 2× EC_{50}. Normalized fold change is indicated as a heatmap. The *P* value for each fold change is <0.05 ($n = 3$). Individual *P* values are reported in Supplementary Table S2.

Published OnlineFirst June 24, 2014; DOI: 10.1158/1078-0432.CCR-14-0072

patient-derived Ewing sarcoma cell lines containing EWS/FLI, we next asked whether the effects were restricted to EWS/FLI-containing lines, or whether they can be generalized to other Ewing sarcoma–associated fusions. As was seen for EWS/FLI-containing cell lines, the Ewing sarcoma cell line TTC-466 containing the alternative EWS/ETS fusion, EWS/ERG, was also sensitive to HCI2509 treatment (Supplementary Fig. S1A). Like A673 cells, TTC-466 cells with EWS/ERG knockdown showed decreased sensitivity to HCI2509. We further tested whether introducing EWS/FLI into a heterologous cell line induced sensitization to HCI2509 treatment in NIH 3T3 fibroblasts (Supplementary Fig. S1B). No sensitization was observed, suggesting EWS/ETS-dependent sensitization is unique to Ewing sarcoma cells.

To assess changes in gene expression caused by LSD1 inhibition in the context of EWS/ETS fusion transcriptional activity, we first generated transcriptional signatures for EWS/FLI and EWS/ERG. A673 and TTC-466 cell lines were subjected to retroviral-mediated shRNA knockdown of EWS/FLI and EWS/ERG, respectively, and the differentially expressed genes were assessed using RNA-seq (A673 data is previously reported; ref. 40). We first analyzed the similarity between EWS/FLI and EWS/ERG transcriptional regulation, and found the overlap between these transcriptional profiles was significant by both χ^2 and GSEA (Supplementary Fig. S1C and S1D).

Having established similarity between the EWS/FLI and EWS/ERG transcriptional profiles, we next determined the global transcriptional signature of HCI2509 using RNA-seq in both A673 and TTC-466 cells. The comparison of the HCI2509 signature with both fusion proteins showed treatment with HCI2509 comprehensively reversed the transcriptional profiles driven by both EWS/FLI (Fig. 1B) and EWS/ERG (Fig. 1C). Thus, genes normally upregulated by EWS/FLI and EWS/ERG were downregulated by LSD1 inhibition with HCI2509, and vice versa. χ^2 analysis showed a statistically significant overlap between EWS/FLI-activated and HCI2509-downregulated genes and vice versa (Supplementary Fig. S1E). This was also true for the TTC-466 cell line (Supplementary Fig. S1F). Importantly, when either EWS/FLI- or EWS/ERG-upregulated target genes were analyzed with HCI2509-upregulated genes, and vice versa, no significant overlap was observed (data not shown). These results suggest substantial reversal of global transcriptional activity of both EWS/ETS fusions and highlights the importance of LSD1 in EWS/ETS-mediated transcriptional dysregulation, for both EWS/ETS-repressed and EWS/ETS-activated genes.

We alternatively compared HCI2509 and EWS/ETS transcriptional profiles using GSEA with a more stringent cutoff of a 4-fold change and FDR of 1×10^{-15} for the EWS/FLI gene set and a 3-fold change and FDR of 1×10^{-10} for the EWS/ERG gene set. The HCI2509 downregulated genes clustered significantly with upregulated EWS/ETS target genes and vice versa (Fig. 1D and E). This confirmed the mechanism of HCI2509 action specifically correlated to the EWS/ETS transcriptional function.

Because EWS/FLI interacts directly with the NuRD/LSD1 complex, we hypothesized the effects of LSD1 inhibition would be observed at genes regulated by direct binding of EWS/FLI. To test this, we compared the HCI2509 regulated gene list to a set of previously identified EWS/FLI direct target genes (38). GSEA showed significant correlation for genes both up- and downregulated directly by EWS/FLI in the HCI2509-regulated gene list (Supplementary Fig. S1G), suggesting that LSD1 is critical to the transcriptional function of EWS/FLI at its direct targets. Since HDAC2 and HDAC3 were previously shown to be directly recruited by EWS/FLI to mediate transcriptional repression (29), we also compared changes in gene expression mediated by the HDAC inhibitor vorinostat (30) to the EWS/FLI direct targets (38). As expected, genes that are directly repressed by EWS/FLI became derepressed with vorinostat treatment (Supplementary Fig. S1H). However, vorinostat had no effect on genes directly activated by EWS/FLI (Supplementary Fig. S1H). Together, these data illustrate that LSD1 inhibition has a unique dual effect in both transcriptional activation and repression mediated by EWS/FLI, whereas targeted inhibition of HDACs only blocks EWS/FLI–mediated transcriptional repression.

We next assessed the functional significance of the HCI2509 and EWS/ETS overlapping gene sets with the Database for Annotation, Visualization, and Integrated Discovery (DAVID). The most significant classes of genes downregulated by HCI2509 are related to DNA replication and cell cycle while the classes of genes upregulated by HCI2509 are related to regulation of cell death and extracellular matrix (Supplementary Fig. S1I and S1J). These are consistent with previously described molecular functions dependent upon EWS/FLI (41). We then used both A673 and TTC-466 cell lines to validate target genes from the HCI2509 RNA-seq profiles which have been identified as EWS/FLI targets critical for oncogenic transformation, survival, and differentiation (31, 42–48). Using quantitative reverse transcriptase PCR (qRT-PCR), genes activated by EWS/FLI, including *NKX2.2*, *CAV1*, *GSTM4*, *E2F1*, and *IGF1*, were all significantly downregulated in both cell lines with HCI2509 treatment. Conversely, genes repressed by EWS/FLI, including *RUNX2*, *IGFBP3*, *CDH1*, and *HMOX1*, were significantly upregulated in both cell lines after treatment (Fig. 1F). Using this 9 gene panel we tested other patient-derived Ewing sarcoma cell lines (EWS-502, SK-N-MC, SKES1, TC-71) to confirm the transcriptional effects of HCI2509 treatment were not cell line specific. Each cell line showed results congruent with A673 and TTC-466 cells (Supplementary Fig. S1K) indicating the disruption of EWS/ETS transcriptional activity by HCI2509 occurs in all tested Ewing sarcoma cell lines.

HCI2509 recapitulates morphologic phenotypes associated with EWS/FLI knockdown

The disruption of EWS/ETS transcriptional activity by HCI2509 should manifest in changes to cellular phenotypes associated with the presence of EWS/ETS. To test this, we first asked whether HCI2509 mimics the morphologic

Published OnlineFirst June 24, 2014; DOI: 10.1158/1078-0432.CCR-14-0072

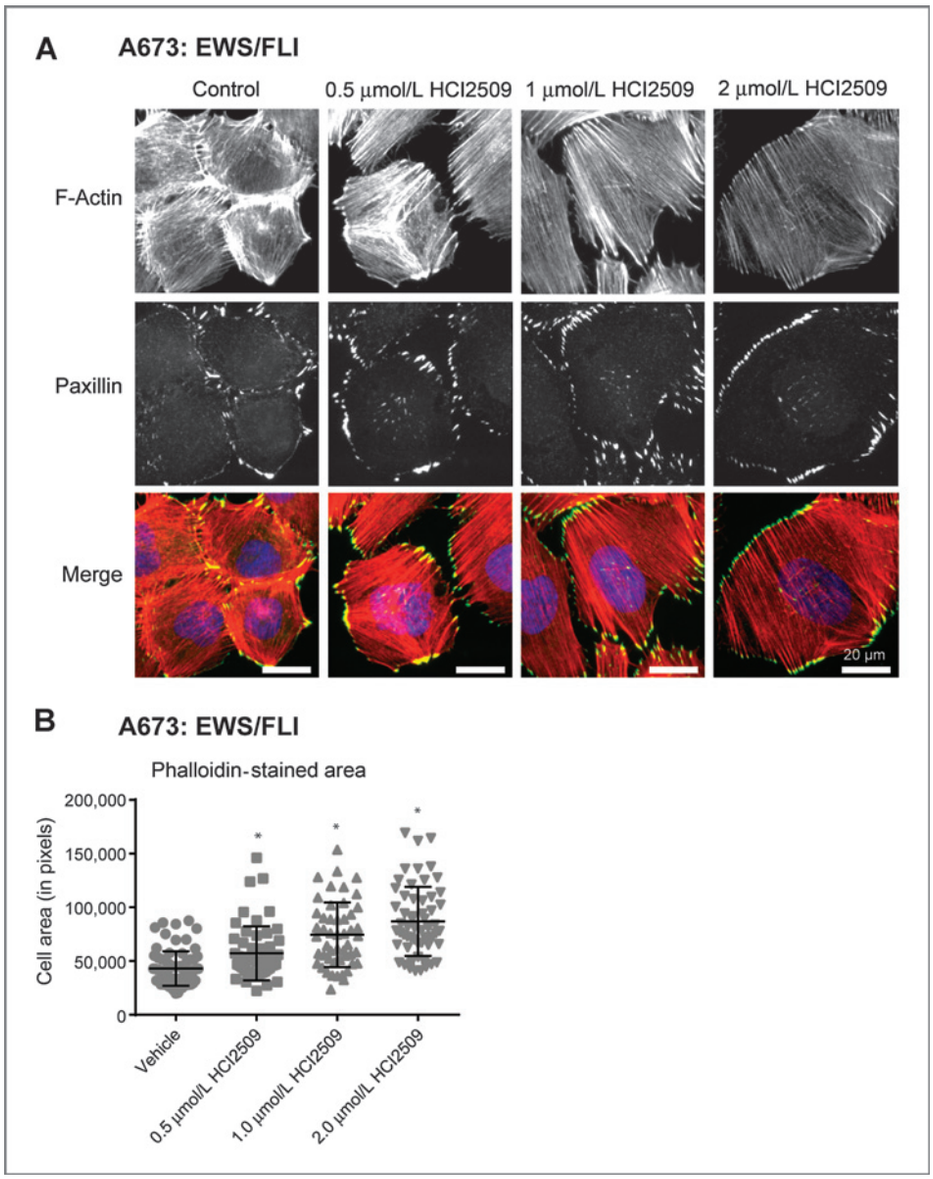

Figure 2. Morphologic changes in A673 with HCI2509 treatment. A, immunofluorescence images of A673 cells treated with increasing doses of HCI2509 for 3 days. Staining was performed for F-actin stress fibers (red–phalloidin) and for focal adhesions (green–paxillin), and nuclei (blue). HCI2509 induced a dose-dependent increase in the cell spreading and morphology. B, cell area in pixels shows a dose-dependent increase in cell spreading with increasing doses of HCI2509. A673 cells were fixed and stained with phalloidin. Cell area was quantified as previously described (39). Data is plotted as Mean with SD and *P* values were calculated using a Student's *t*-test (*, $P < 0.0001$).

phenotypes associated with EWS/ETS knockdown. Ewing sarcoma is characterized histologically by small round blue-staining cells. In the context of EWS/FLI knockdown, cells display morphologic phenotypes typical of the putative mesenchymal stem cell cell-of-origin (39). EWS/FLI knockdown induces a robust actin cytoarchitecture with striking actin stress fibers anchored to integrin-based focal adhesions, increased cell adhesion, and spreading, that correlated with increased migration (39). To assess the effect of HCI2509 on cellular architecture, we performed immunofluorescence microscopy. Control A673 cells showed the characteristic small round cell phenotype of Ewing sarcoma with short, thin actin fibers (Fig. 2A and Supplementary Fig. S2A). Treatment with HCI2509 induced organizing of actin stress fibers throughout a well-spread cell, with robust paxillin-containing focal adhesions (Fig. 2A and Supplementary Fig. S2A). Cell area of the phalloidin-stained cells was measured to quantify the effect. HCI2509-treated A673 cells showed a dose-dependent increase in cell area (Fig. 2B). To show observed morphologic changes were on target, we knocked down LSD1 using siRNA and assessed both cytoskeletal architecture and cell area. Consistent with the increased cell spreading phenotypes we observed with HCI2509 treatment, decreased LSD1 protein levels correlated with increased cell spreading (Supplementary Fig. S2B and S2C). TTC-466 likewise showed dose-dependent changes in actin staining, focal adhesions, and cell spreading (Supplementary Fig. S2D–S2F), suggesting treatment with HCI2509 generated the morphology associated with the loss of EWS/FLI.

Published OnlineFirst June 24, 2014; DOI: 10.1158/1078-0432.CCR-14-0072

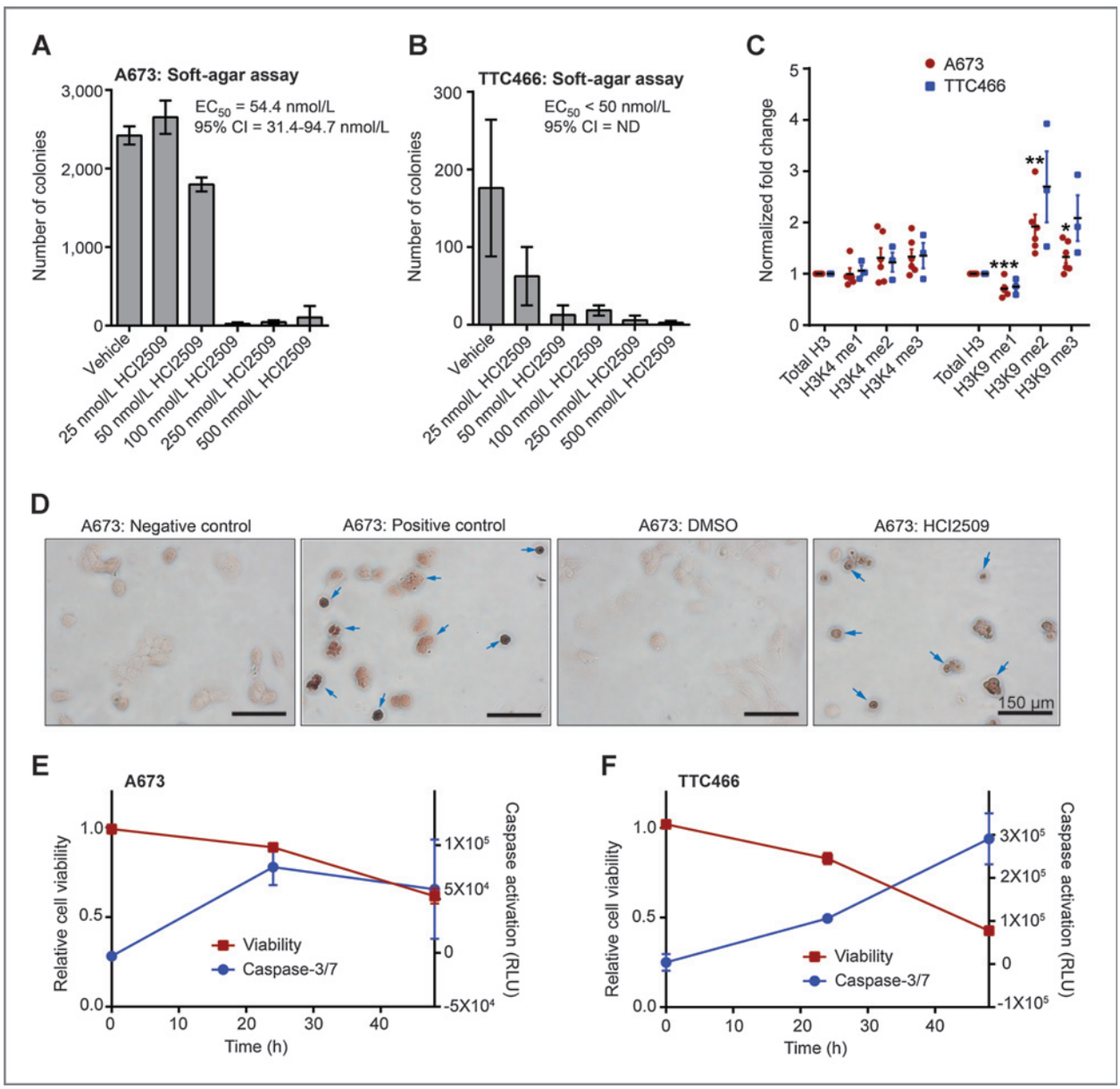

Figure 3. Mechanism of action of HCI2509 *in vitro*. A and B, quantification of colonies formed by (A) A673 cells and (B) TTC-466 cells treated with either vehicle (0.3% DMSO) or increasing doses of HCI2509. Error bars indicate SD of duplicate assays. EC_{50} values were determined using GraphPad Prism 6. C, quantification of global methylation changes at histone H3K4 and H3K9 in A673 (red, $n = 5$) and TTC-466 (blue, $n = 3$) following 48-hour treatment with 2 μmol/L HCI2509. Methyl marks were assayed by Western blot analysis and the relative band intensities were quantified using ImageQuant (GE Healthcare Biosciences). Each sample was normalized to total H3 and fold change was determined in comparison with a vehicle control. Error bars indicate SEM and *P* values were calculated using a Student's *t*-test (*, $P = 4.25E{-}2$; **, $P = 1.07E{-}2$; ***, $P = 6.36E{-}3$). D, TUNEL staining of A673 cells treated with either vehicle (0.3% DMSO) or 2 μmol/L HCI2509. Negative control indicates lack of labeling and positive control indicates DNase treatment with labeling. Arrows indicated TUNEL-positive cells. E and F, cell viability and caspase activation at 0, 24, and 48 hours in A673 (E) and TTC-466 cells (F) treated with 2 μmol/L HCI2509. Measurements were normalized to their respective vehicle (0.3% DMSO) sample at the appropriate time point.

HCI2509 affects oncogenic transformation, histone methylation, and causes apoptosis

We next tested whether HCI2509 would impair EWS-ETS-driven oncogenic transformation using colony formation assays as a measure of anchorage-independent growth (Fig. 3A and B and Supplementary Fig. S3A–S3C). Interestingly, both the A673 and TTC-466 showed a shift in sensitivity (Fig. 3A and B) to the low nanomolar range in three-dimensional cultures. Thus, the EC_{50} observed was significantly lower than those seen in viability assays (29).

Given the role of LSD1 in H3K4 and H3K9 demethylation, we also characterized changes in global histone methylation at these residues (Fig. 3C). Immunodetection of methylation status was quantified using densitometry for

Published OnlineFirst June 24, 2014; DOI: 10.1158/1078-0432.CCR-14-0072

statistical analysis. Due to the subtlety of the observed changes, several biologic replicates were performed. Interestingly, A673 cells showed no change in H3K4 monomethylation, and while H3K4 dimethylation (H3K4me2) and trimethyation (H3K4me3) trended higher, the effect was not statistically significant (Fig. 3C). However, H3K9 monomethylation (H3K9me1) significantly decreased, with a complementary increase in H3K9 dimethylation (H3K9me2) and trimethylation (H3K9me3; Fig. 3C). TTC-466 cells generally recapitulated the effects seen in A673 (Fig. 3C), but the results showed more variability.

We used DAVID analysis to examine the functional relevance of HCI2509 differentially expressed genes apart from the overlap with the EWS/FLI transcriptional profile (Supplementary Fig. S1E). Notably, genes upregulated by HCI2509 related to cell-cycle arrest and programmed cell death, while downregulated genes associated with S-phase, cell cycle, and proliferation (data not shown). Thus, HCI2509 likely reduces Ewing sarcoma cell viability (29) through induction of apoptosis. We therefore used TUNEL staining and caspase activation to assay whether HCI2509 triggered apoptosis. TUNEL-stained cells treated with HCI2509 for 48 hours showed increased staining as compared with vehicle (Fig. 3D). Similarly, treatment with HCI2509 showed increased activation of caspase-3/7 over 48 hours, which corresponded with decreased viability in multiple Ewing sarcoma cell lines (Fig. 3E and F and Supplementary Fig. S3D–S3F). Collectively, these data show HCI2509 not only reversed EWS/FLI-associated oncogenic phenotypes, but also altered H3K9 methylation status and induced apoptosis.

HMOX1 is an on-target response biomarker for HCI2509 treatment *in vitro*

Screening efforts to identify HCI2509 (33) suggested induction of *HMOX1* was an effect proportional to the biochemical potency of the inhibitor (Supplementary Fig. S4A). We evaluated whether *HMOX1* constituted biologic output to demonstrate target engagement. *HMOX1* was significantly upregulated by HCI2509 in both EWS/ETS transcriptional profiles. We assessed the regulation of *HMOX1* by alternative EWS/ETS fusions and found *HMOX1* was repressed across EWS/ETS fusions (Fig. 4A). Moreover, Venn Master analysis revealed *HMOX1* was one of 81 genes present in the overlap between EWS/FLI targets upregulated by HCI2509 and genes downregulated by EWS/FLI in primary Ewing sarcoma samples (ref. 41; Fig. 4B). On the basis of the repression of *HMOX1* in primary tumors and robust HCI2509-induced derepression across tested cell lines, we asked whether HMOX1 protein also increased. We found HMOX1 protein levels elevated with EWS/FLI knockdown returned to baseline levels with EWS/FLI re-expression (Fig. 4C) and likewise increased in response to HCI2509 (Fig. 4D).

We next asked whether *HMOX1* induction was dependent upon both LSD1 and EWS/FLI function. Targeted LSD1 ChIP showed enrichment at the *HMOX1* promoter (Fig. 4E). Both siRNA-mediated knockdown of LSD1 and LSD1 inhibition with HCI2509 derepressed *HMOX1* in a dose-dependent manner (Fig. 4F and G). Moreover, this dose-dependent increase was validated at the protein level using ELISA (Fig. 4H). EWS/FLI knockdown resulted in similar *HMOX1* induction as 100 nmol/L LSD1 siRNA (Fig. 4I). *HMOX1* repression was restored with full-length EWS/FLI rescue; however, rescue with either the Δ22 mutant (49) lacking most of the EWS domain or the DNA-binding mutant R2L2 (50) failed to repress *HMOX1* (Fig. 4I and Supplementary Fig. S4B). This is consistent with other EWS/FLI-repressed targets (29), and jointly implicates the repressive function of the EWS domain together with the DNA-binding domain of FLI in suppressing *HMOX1* expression.

The necessity of the EWS domain raised the question about which corepressor complex EWS/FLI recruits to repress *HMOX1*. EWS/FLI is known to recruit the NuRD complex to enact repressive transcriptional activity at some target genes (29) so we first probed whether NuRD was responsible for *HMOX1* repression. Knockdown of the NuRD complex with CHD4-RNAi induced a 4.5-fold increase in *HMOX1* (Fig. 4J). RNAi-mediated knockdown of the REST, Co-REST, NcoR/SMRT, and Sin3A complexes were also evaluated. Only REST knockdown showed a significant, though lower magnitude, increase in *HMOX1* mRNA (Supplementary Fig. S4C). These results are consistent with recruitment of LSD1 by REST (51), but highlight the central role of the NuRD complex in repressing *HMOX1*.

Because HMOX1 protein was strongly induced in cells treated with HCI2509 in addition to those with EWS/FLI knockdown, we investigated whether HMOX1 affects cellular transformation. A673 cells overexpressing HMOX1 (Supplementary Fig. S4D) showed little difference in doubling times compared with control (Supplementary Fig. S4E). In addition, oncogenic transformation was not affected in cells overexpressing HMOX1 (Supplementary Fig. S4F). These findings support a model in which *HMOX1* is directly repressed by EWS/FLI-mediated recruitment of the NuRD complex with its associated LSD1 subunit, but does not play a role in proliferation or the oncogenic phenotype. Thus, in Ewing sarcoma HMOX1 is a useful biologic readout of LSD1 inhibition and associated disruption of EWS/ETS transcriptional activity.

HCI2509 as a single agent significantly reduces tumor growth *in vivo*

Having observed HCI2509-mediated disruption of global EWS/ETS transcriptional function, reversal of EWS/ETS-associated morphologic and oncogenic phenotypes, and induction of apoptosis, we next investigated whether HCI2509 would impair tumorigenesis *in vivo*. In A673, SK-N-MC, and SKES1 xenograft models, daily intraperitoneal treatment with 30 mg/kg HCI2509 delayed tumor growth as a single agent (Fig. 5A and B and Supplementary Fig. S5A). Animal weights were recorded to monitor nonspecific toxicity with none observed (Supplementary Fig. S5B–S5D). Blood counts were also examined due to

Published OnlineFirst June 24, 2014; DOI: 10.1158/1078-0432.CCR-14-0072

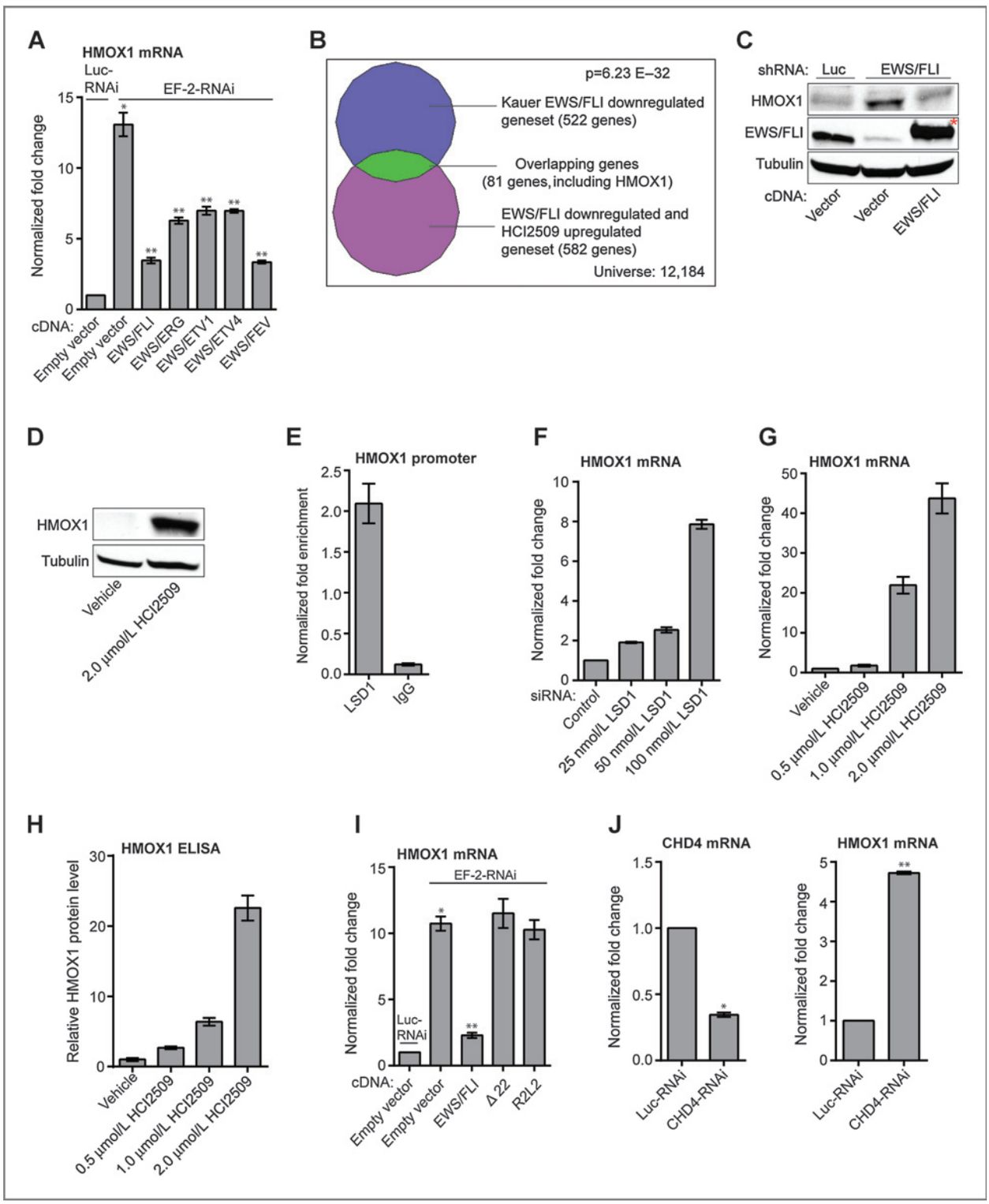

Figure 4. Regulation of HMOX1. A, validation of *HMOX1* as a target gene of multiple EWS/ETS fusion. qRT-PCR analysis of *HMOX1* in A673 cells infected with a control shRNA (Luc) or an EWS/FLI shRNA followed by rescue with an empty vector, an RNAi-resistant EWS/FLI, EWS/ETV1, EWS/ERG, EWS/ETV4, or EWS/FEV cDNA. Error bars indicate SD ($n = 3$). *P* values were calculated using Student's *t*-test. *, *P* value determined against Luc-RNAi/Empty vector ($P = 1.51E{-}5$). **, *P* values determined against EF-2-RNAi/Empty vector ($P \leq 2.79E{-}4$). B, Venn diagram representation of the HCI2509-upregulated and EWS/FLI-downregulated gene set (from Supplementary Fig. S1E) overlapped with EWS/FLI-downregulated targets in primary tissue samples. The χ^2 determined *P* value is indicated. (*Continued on the following page.*)

Published OnlineFirst June 24, 2014; DOI: 10.1158/1078-0432.CCR-14-0072

hematopoietic toxicity associated with LSD1 knockdown (52). During 4 weeks of treatment, no significant difference was observed between vehicle and treated groups (Supplementary Fig. S5E). Importantly, animals treated with HCI2509 showed improved survival over 60 days (Fig. 5C and D) as compared with vehicle in both A673 and SK-N-MC xenograft models.

We also evaluated HMOX1 in tumors from the A673 study using 6 tumors from the vehicle group and 6 tumors from the treatment group. *HMOX1* RNA was elevated in three treatment tumors as compared with the control tumors (Fig. 5E). Moreover, this result was validated at the protein level with HMOX protein nearly undetectable in three representative control tumors and expressed in all three HCI2509-treated tumors with elevated *HMOX1* mRNA (Fig. 5F). This suggested HCI2509 both engages LSD1 and disrupts EWS/FLI transcriptional activity *in vivo*. When considered with the impaired tumorigenesis and increased survival, these data substantiate LSD1 inhibition with HCI2509 as a potential therapeutic strategy for Ewing sarcoma.

Discussion

Our findings reveal a novel dual role for LSD1 in mediating both the transcriptional activating and repressive function of EWS/ETS fusions in Ewing sarcoma and modulating the oncogenic phenotypes resulting from the presence of EWS/ETS fusions proteins. Small-molecule blockade of LSD1 with the potent and reversible inhibitor, HCI2509, comprehensively disrupted the transcriptional signature of EWS/FLI and EWS/ERG as well as the subsequent downstream malignant characteristics of Ewing sarcoma cells as depicted in Fig. 6. Transcription factors are notoriously difficult targets for drug discovery and development programs and identification of small molecules which disrupt EWS/FLI has been an elusive goal (53). Recently, disruption of the c-Myc oncogenic transcription factor was achieved through targeted inhibition of the epigenetic reader BRD4 with the small-molecule inhibitor JQ1, which downregulated *MYC* transcription, decreased c-Myc protein, and disrupted c-Myc transcriptional function (54, 55). Our results likewise support an approach undermining oncogenic transcription factors by targeting their associated epigenetic machinery. The observed difference in transcriptional outcomes between LSD1 inhibition and HDAC inhibition with vorinostat (30) highlights the importance of selecting the correct target and demonstrates the potential to tailor epigenetic therapy based on the context of the disease.

The A673 cell line has been used to investigate the transcriptional effects of EWS/FLI because it is relatively tolerant of EWS/FLI knockdown (31). While A673 cells expressing EWS/FLI shRNA lose transformation (31) and show morphologic characteristics similar to the putative cell-of-origin for Ewing sarcoma (39), cell growth and viability are not impaired. HCI2509 treatment largely reproduced the loss of transformation consistent with downregulation of EWS/ETS-activated targets and upregulation of EWS/ETS-repressed targets. However, unlike EWS/FLI knockdown, treatment with HCI2509 triggered caspase-dependent apoptosis in A673 cells. This effect was consistent across cell lines, suggesting additional mechanisms of action for HCI2509. Upon analysis of the genes regulated by HCI2509, but not overlapping with the EWS/FLI transcriptional profile we noted that in this context, HCI2509 upregulated genes associated with cell-cycle arrest and programmed cell death, while genes associated with S-phase, cell cycle, and proliferation were downregulated. This is consistent with both the observed apoptotic phenotype and the reported role for LSD1 in the maintenance of dedifferentiation in cancer (16–19, 56) and regulation of the cell cycle in stem-like cells (57–60). In addition, LSD1 is known to regulate non-histone proteins, including p53 (61). LSD1-mediated demethylation of p53 disrupts association of its cofactor 53BP1 and prevents induction of apoptosis (61). Thus, the sensitivity of Ewing sarcoma cell lines to LSD1 inhibition with HCI2509 may be the result of two tiers of LSD1-specific effects and this is reflected in the different EC_{50}s of the phenotypes described with treatment. Sankar and colleagues previously reported the EC_{50} for HCI2509 in cell viability assays for multiple Ewing sarcoma cell lines ranging from 0.19 to 1.4 μmol/L (29). In this report, both A673 and TTC-466 cell lines show a loss of transformation in colony forming assays below 100 and 50 nmol/L of HCI2509 treatment, respectively. This suggests a model for HCI2509 mechanism of action in Ewing sarcoma where the first tier of effects disrupt the transforming function of EWS/ETS at concentrations much lower than the second tier of effects, which result in induction of apoptosis. Nonetheless, the proapoptotic effects of HCI2509 may be due to as yet undescribed off-target effects. However, we feel this is unlikely, as the only off-target for HCI2509 known to us is mild inhibition of CYP3A4 with a biochemical IC_{50} of 2.61 μmol/L (33).

(*Continued.*) C and D, Western blot analysis of HMOX1 protein levels with EWS/FLI knockdown/rescue (B) and HCI2509 treatment (C). HMOX1 and EWS/FLI levels were assessed in A673 cells using anti-HMOX1 and anti-FLI antibodies. Tubulin was used as a loading control. (*) indicates the 3x-FLAG–tagged EWS/FLI cDNA that runs slightly higher than endogenous EWS/FLI. E, ChIP of LSD1 with the level of enrichment for LSD1 at the *HMOX1* transcription start site plotted as normalized fold enrichment compared with the enrichment at *BCL2L1* as a negative control. IgG was used as a negative antibody control. The error bars indicate SEM ($n = 3$). The Student's *t*-test determined *P* value is 1.10E−3. F–J, validation of *HMOX1* repression as on target. *P* values were calculated using a Student's *t*-test. qRT-PCR analysis of *HMOX1* in A673 cells treated with: vehicle (F), 25 nmol/L ($P = 1.43E-5$), 50 nmol/L ($P = 3.05E-4$), and 100 nmol/L LSD1 siRNA ($P = 7.39E-6$) and vehicle (G), 0.5 μmol/L ($P = 3.65E-2$), 1 μmol/L (5.82E−4), and 2 μmol/L HCI2509 (3.48E−4). H, quantification of protein levels by ELISA for A673 cells treated with vehicle, 0.5 μmol/L ($P = 6E-4$), 1 μmol/L ($P = 1E-4$), and 2 μmol/L HCI2509 ($P = 1E-4$). I, qRT-PCR analysis of *HMOX1* in A673 cells treated with (I) knockdown of EWS/FLI and rescue with full-length, Δ22, and R2L2 mutants. *, *P* value determined against Luc-RNAi/Empty vector ($P = 1.32E-6$). **, *P* value determined against EF-2-RNAi/Empty vector ($P = 3.99E-6$). J, qRT-PCR analysis of both *CHD4* and *HMOX1* mRNA in the presence of control or CHD4 RNAi. *, $P = 2.95E-7$; **, $P = 3.98E-9$. Error bars indicate SD ($n = 3$).

Published OnlineFirst June 24, 2014; DOI: 10.1158/1078-0432.CCR-14-0072

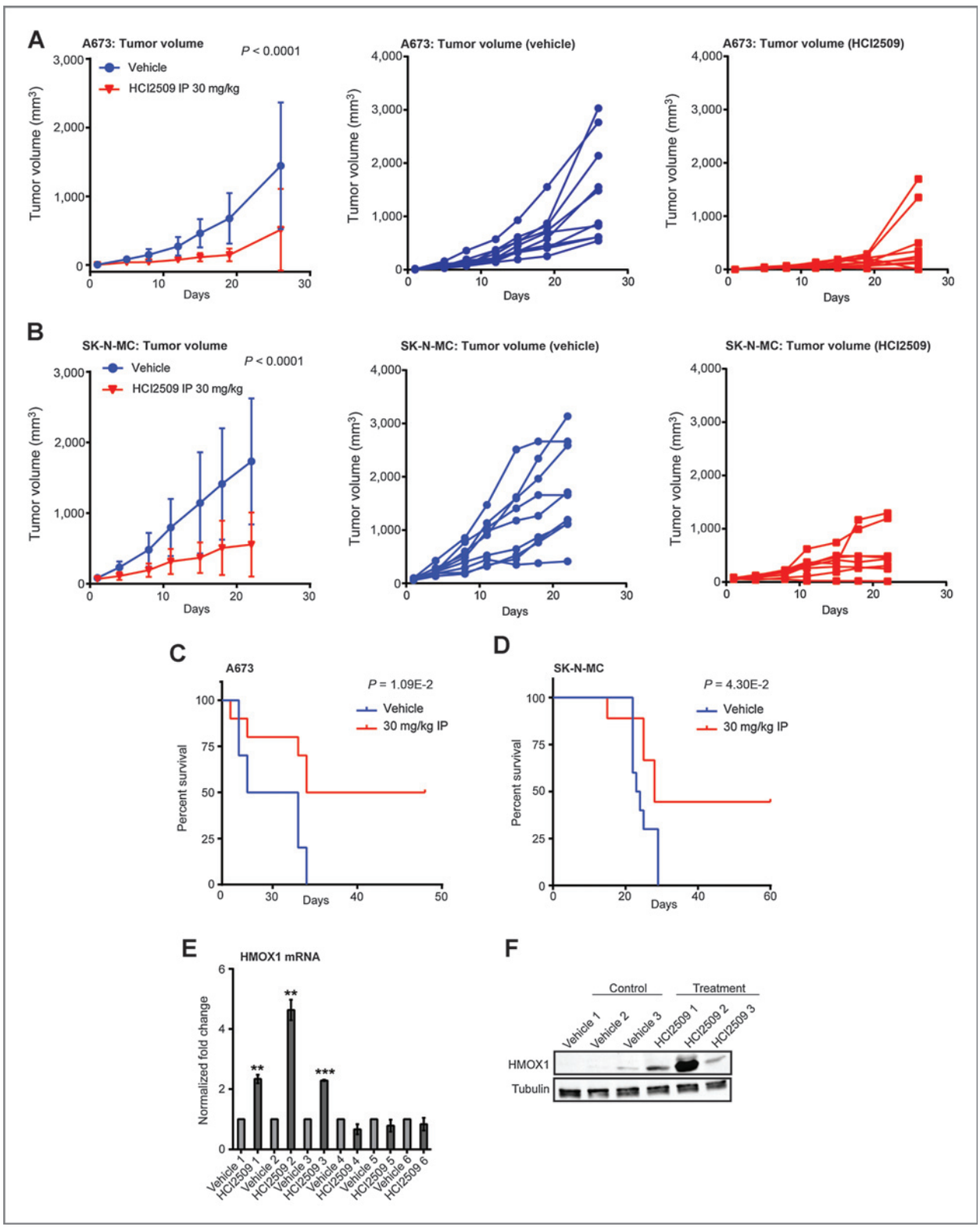

Figure 5. HCI2509 activity *in vivo*. A and B, *in vivo* subcutaneous hind-flank xenograft studies measuring tumor volume for animals bearing tumors grown from (A) A673 cells and (B) SK-N-MC cells. N = 10 for all groups, with the exception of SK-N-MC HCI2509–treated group as noted. For tumor volumes, *P* values were determined by two-way ANOVA comparing the treatment curve to the vehicle curve. Individual tumor growth curves are shown for the vehicle-treated (blue) and HCI2509-treated (red) groups. (*Continued on the following page.*)

Published OnlineFirst June 24, 2014; DOI: 10.1158/1078-0432.CCR-14-0072

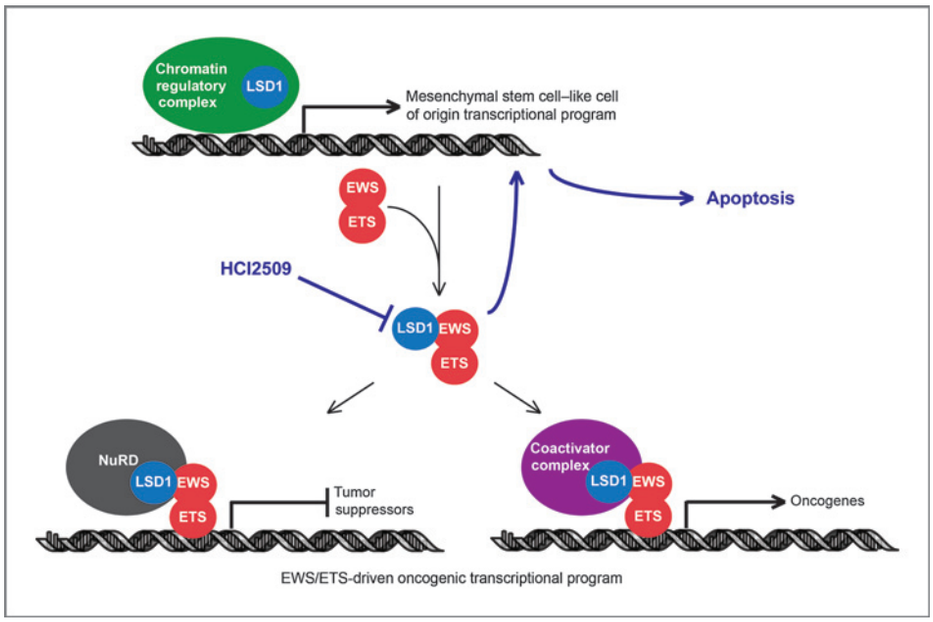

Figure 6. Model for HCI2509 mechanism of action in Ewing sarcoma. HCI2509 treatment inhibits LSD1, which impairs the ability of EWS/ETS fusions proteins to globally alter gene expression. This leads, in part, to a reversion to the transcriptional program of the putative cell-of-origin and causes apoptosis.

Given its known capability to demethylate both H3K4 and H3K9 mono- and dimethyl marks, and its dual role in modulating activated and repressed genes, we were surprised to observe the only significant changes in global histone methylation occurring at the H3K9 residue. Methylation at H3K9 is typically associated with gene repression so this may be linked to the apparent role of LSD1 in EWS/ETS-mediated gene activation. LSD1-mediated demethylation of MTA1 causes a switch in the associated complex from the repressive NuRD complex to the activated NURF complex (62). In turn, NURF directs the demethylase activity of LSD1 toward H3K9 (62). This presents a plausible mechanism by which EWS/FLI recruits LSD1 as a member of the NuRD complex and is then able to enact both transcriptional activation and repression. Alternatively, LSD1 was recently described to mediate a global reduction in H3K9me2 during the epithelial-to-mesenchymal transition (EMT; ref. 63). Inhibition of LSD1 in this model impaired the cellular migration and chemoresistance resulting from EMT. It is possible that the observed increase in H3K9me2 in Ewing sarcoma cells may be due to a similar phenomenon. Additional studies are required to elucidate the molecular mechanisms choreographing whether LSD1 facilitates EWS/FLI-mediated transcriptional activation or repression and the genome-wide positioning of LSD1 histone substrates in the presence and absence of both EWS/FLI and HCI2509. The absence of significant changes at the H3K4 mark may be due to limitations of our study design to assay global histone marks at the same time point as the transcriptional profiling. In embryonic stem cells, LSD1 was shown to mediate short-term changes at H3K4 important for cell-cycle progression and these changes may not have been observed in global methylation analyses at 48 hours (58).

Ewing sarcoma is an aggressive cancer for which few agents show single-agent efficacy *in vivo*. We assessed *HMOX1* induction in the A673 study and while most animals in the treatment group had delayed tumorigenesis, the endpoint study design did not allow us to assay *HMOX1* levels during earlier time points of treatment. Importantly, we were able to observe induction of *HMOX1* in a subset of tumors from the treated group as compared with the vehicle group. On the basis of our *in vitro* results we expected to see a more robust *HMOX1* induction in the context of antitumor efficacy. While the presence of an EWS/ETS fusion may predict a favorable response to an LSD1 inhibitor, these results underscore the difficulty in identifying of appropriate treatment response biomarkers in Ewing sarcoma.

On the basis of the dramatic transcriptional effects of HCI2509 described *in vitro*, we predict improved dosing will result in enhanced tumor regression in future studies with this class of LSD1 inhibitors. This is a critical hurdle for translation of this strategy to the clinic for Ewing sarcoma. Even with a preliminary preclinical formulation we were

(*Continued.*) C and D, survival curves for mice bearing subcutaneous hind-flank xenografts of A673 cells (C) or SK-N-MC cells (D). N = 10 for the A673 group. In the SK-N-MC treatment group, one mouse died due to a treatment-unrelated rash and was censored from further analysis. Therefore, in the SK-N-MC study, 10 and 9 mice were used for the vehicle and HCI2509 treatment groups, respectively. The mice were sacrificed once their tumors reached a size limit of 2 cm^3. Percent survival was plotted as Kaplan–Meier survival curves using GraphPad Prism. The log-rank (Mantel–Cox Test) determined *P* values using GraphPad Prism are indicated. E and F, analysis of HMOX1 expression by qRT-PCR (E) and Western blot analysis (F) in tumors from both vehicle and treatment A673 groups. Only the three tumors which showed an increase in *HMOX1* RNA (E) were used for Western blotting with three random vehicle tumors (F). HMOX1 levels were assessed using an anti-HMOX1 antibody. Tubulin was used as a loading control. Error bars indicate SD (*, $P < 0.01$; **, $P < 0.001$).

Published OnlineFirst June 24, 2014; DOI: 10.1158/1078-0432.CCR-14-0072

able to observe significant delay in tumor growth and improved survival out to 60 days. Optimization of formulation, salt forms, and synthesis of more soluble derivatives will allow fine tuning of drug exposure. Future studies are required to optimize dosing and determine whether or not LSD1 inhibition with HCI2509 is safe, tolerated, and synergistic with other clinically relevant treatment strategies for Ewing sarcoma, like irinotecan and temozolomide. Taken together, the dramatic effects of HCI2509 on the transcriptional activity of EWS/ETS fusions and its observed single-agent efficacy *in vivo* validate this class of LSD1 inhibitors as a potential targeted strategy to treat Ewing sarcoma.

Disclosure of Potential Conflicts of Interest

S. Sharma is an employee of and holds ownership interest (including patents) in Salarius Pharmaceuticals. S.L. Lessnick is a consultant/advisory board member for Salarius Pharmaceuticals. No potential conflicts of interest were disclosed by the other authors.

Authors' Contributions

Conception and design: S. Sankar, E.R. Theisen, M. Beckerle, S. Sharma, S.L. Lessnick
Development of methodology: S. Sankar, E.R. Theisen, S. Sharma, S.L. Lessnick
Acquisition of data (provided animals, acquired and managed patients, provided facilities, etc.): S. Sankar, E.R. Theisen, J. Bearss, T. Mulvihill, L.M. Hoffman
Analysis and interpretation of data (e.g., statistical analysis, biostatistics, computational analysis): S. Sankar, E.R. Theisen, S.L. Lessnick
Writing, review, and/or revision of the manuscript: S. Sankar, E.R. Theisen, L.M. Hoffman, V. Sorna, M. Beckerle, S. Sharma, S.L. Lessnick
Administrative, technical, or material support (i.e., reporting or organizing data, constructing databases): S. Sankar
Study supervision: M. Beckerle, S.L. Lessnick
Other (design and synthesis of the novel molecule used for this manuscript): V. Sorna

Grant Support

S.L. Lessnick was supported by NIH/NCI grant R01 CA140394. S.L. Lessnick and S. Sharma were supported by a Developmental Research Program subaward from the SARC Sarcoma SPORE (U54 CA168512), The Sunshine Project from the Pediatric Cancer Foundation, the Make Some Noise: Cure Kids Cancer Foundation, and the Alan B. Slifka Foundation. S. Sankar was supported by the HHMI Med into Grad program at the University of Utah (U2M2G), E.R. Theisen was supported by the American Foundation for Pharmaceutical Education 2013 Pre-Doctoral Fellowship (AFPE), and T. Mulvihill was supported by the University of Utah MD/PhD Program. L.M. Hoffman and M. Beckerle were supported by NIH grant R01 GM50877. The authors also acknowledge support of funds in conjunction with NCI grant P30 CA042014 awarded to the Huntsman Cancer Institute, as well as funds from the Experimental Therapeutics Program at Huntsman Cancer Institute.

The costs of publication of this article were defrayed in part by the payment of page charges. This article must therefore be hereby marked *advertisement* in accordance with 18 U.S.C. Section 1734 solely to indicate this fact.

Received January 10, 2014; revised May 15, 2014; accepted June 10, 2014; published OnlineFirst June 24, 2014.

References

1. Dawson MA, Kouzarides T, Cancer epigenetics: from mechanism to therapy. Cell 2012;150:12–27.
2. Sharma S, Kelly TK, Jones PA. Epigenetics in cancer. Carcinogenesis 2010;31:27–36.
3. Lachner M, O'Sullivan RJ, Jenuwein T. An epigenetic road map for histone lysine methylation. J Cell Sci 2003;116:2117–24.
4. Stresemann C, Lyko F. Modes of action of the DNA methyltransferase inhibitors azacytidine and decitabine. Int J Cancer 2008;123:8–13.
5. Choudhary C, Kumar C, Gnad F, Nielsen ML, Rehman M, Walther TC, et al. Lysine acetylation targets protein complexes and co-regulates major cellular functions. Science 2009;325:834–40.
6. Kubicek S, Gilbert JC, Fomina-Yadlin D, Gitlin AD, Yuan Y, Wagner FF, et al. Chromatin-targeting small molecules cause class-specific transcriptional changes in pancreatic endocrine cells. Proc Natl Acad Sci USA 2012;109:5364–69.
7. Islam AB, Richter WF, Lopez-Bigas N, Benevolenskaya EV, Selective targeting of histone methylation. Cell Cycle 2011;10:413–24.
8. Popovic R, Licht JD, Emerging epigenetic targets and therapies in cancer medicine. Cancer Discov 2012;2:405–13.
9. McCabe MT, Ott HM, Ganji G, Korenchuk S, Thompson C, Van Aller GS, et al. EZH2 inhibition as a therapeutic strategy for lymphoma with EZH2-activating mutations. Nature 2012;492:108–12.
10. Popovic R, Zeleznik-Le NJ. MLL: How complex does it get? J Cell Biochem 2005;95:234–42.
11. Hormaeche I, Licht JD. Chromatin modulation by oncogenic transcription factors: new complexity, new therapeutic targets. Cancer Cell 2007;11:475–78.
12. Yoshimi A, Kurokawa M. Key roles of histone methyltransferase and demethylase in leukemogenesis. J Cell Biochem 2011;112:415–24.
13. Hudlebusch HR, Santoni-Rugiu S, Simon R, Ralfkiær E, Rossing HH, Johansen JV, et al. The histone methyltransferase and putative oncoprotein MMSET is overexpressed in a large variety of human tumors. Clin Cancer Res 2011;17:2919–33.
14. Bernt KM, Zhu N, Sinha AU, Vempati S, Faber J, Krivtsov AV, et al. MLL-rearranged leukemia is dependent on aberrant H3K79 methylation by DOT1L. Cancer Cell 2011;20:66–78.
15. Tian X, Zhang S, Liu H-M, Zhang Y-B, Blair CA, Mercola D, et al. Histone lysine-specific methyltransferases and demethylases in carcinogenesis: new targets for cancer therapy and prevention. Curr Cancer Drug Targets 2013;13:558–79.
16. Schulte JH, Lim S, Schramm A, Friedrichs N, Koster J, Versteeg R, et al. Lysine-specific demethylase 1 is strongly expressed in poorly differentiated neuroblastoma: implications for therapy. Cancer Res 2009;69:2065–71.
17. Harris WJ, Huang X, Lynch JT, Spencer GJ, Hitchin JR, Li Y, et al. The histone demethylase KDM1A sustains the oncogenic potential of MLL-AF9 leukemia stem cells. Cancer Cell 2012;21:473–87.
18. Lim S, Janzer A, Becker A, Zimmer A, Schüle R, Buettner R, et al. Lysine-specific demethylase 1 (LSD1) is highly expressed in ER-negative breast cancers and a biomarker predicting aggressive biology. Carcinogenesis 2010;31:512–520.
19. Kahl P, Gullotti L, Heukamp LC, Wolf S, Friedrichs N, Vorreuther R, et al. Androgen receptor coactivators lysine-specific histone demethylase 1 and four and a half LIM domain protein 2 predict risk of prostate cancer recurrence. Cancer Res 2006;66:11341–7.
20. Hayami S, Kelly JD, Cho H-S, Yoshimatsu M, Unoki M, Tsunoda T, et al. Overexpression of LSD1 contributes to human carcinogenesis through chromatin regulation in various cancers. Int J Cancer 2011;128:574–86.
21. Zhao Z-K, Yu H-F, Wang DR, Dong P, Chen L, Wu W-G, et al. Overexpression of lysine specific demethylase 1 predicts worse prognosis in primary hepatocellular carcinoma patients. World J Gastroenterol 2012;18:6651–6.
22. Schildhaus H-U, Riegel R, Hartmann W, Steiner S, Wardelmann E, Merkelbach-Bruse S, et al. Lysine-specific demethylase 1 is highly expressed in solitary fibrous tumors, synovial sarcomas, rhabdomyosarcomas, desmoplastic small round cell tumors, and malignant peripheral nerve sheath tumors. Hum Pathol 2011;42:1667–75.
23. Bennani-Baiti I-M, Machado I, Llombart-Bosch A, Kovar H. Lysine-specific demethylase 1 (LSD1/KDM1A/AOF2/BHC110) is expressed and is an epigenetic drug target in chondrosarcoma, Ewing's

Published OnlineFirst June 24, 2014; DOI: 10.1158/1078-0432.CCR-14-0072

sarcoma, osteosarcoma, and rhabdomyosarcoma. Hum Pathol 2012;43:1300–7.
24. Delattre O, Zucman J, Plougastel B, Desmaze C, Melot T, Peter M, et al. Gene fusion with an ETS DNA-binding domain caused by chromosome translocation in human tumours. Nature 1992;359:162–5.
25. Sankar S, Lessnick SL. Promiscuous partnerships in Ewing's sarcoma. Cancer Genet 2011;204:351–65.
26. Linabery AM, Ross JA. Childhood and adolescent cancer survival in the U.S. by race and ethnicity (diagnostic period 1975–1999). Cancer 2008;113:2575–96.
27. Randall RL, Lessnick SL, Jones KB, Gouw LG, Cummings JE, Cannon-Albright L, et al. Is there a predisposition gene for Ewing's sarcoma? J Oncol 2010;2010:397632.
28. D'Adamo DR, Appraising the current role of chemotherapy for the treatment of sarcoma. Semin Oncol 2011;38 Suppl 3:S19–29.
29. Sankar S, Bell R, Stephens B, Zhuo R, Sharma S, Bearss DJ, et al. Mechanism and relevance of EWS/FLI-mediated transcriptional repression in Ewing sarcoma. Oncogene 2012;32:5089–100.
30. Owen LA, Kowalewski AA, Lessnick SL, EWS/FLI mediates transcriptional repression via NKX2.2 during oncogenic transformation in Ewing's sarcoma. PLoS ONE 2008;3:e1965.
31. Smith R, Owen LA, Trem DJ, Wong JS, Whangbo JS, Golub TR, et al. Expression profiling of EWS/FLI identifies NKX2.2 as a critical target gene in Ewing's sarcoma. Cancer Cell 2006;9:405–16.
32. Braunreiter CL, Hancock JD, Coffin CM, Boucher KM, Lessnick SL. Expression of EWS-ETS fusions in NIH3T3 cells reveals significant differences to Ewing's sarcoma. Cell Cycle 2006;5:2753–9.
33. Sorna V, Theisen ER, Stephens B, Warner SL, Bearss DJ, Vankayalapati H, et al. High-throughput virtual screening identifies novel N'-(1-phenylethylidene)-benzohydrazides as potent, specific, and reversible inhibitors of LSD1. J Med Chem 2013;56:9496–508.
34. Kinsey M, Smith R, Lessnick SL. NR0B1 is required for the oncogenic phenotype mediated by EWS/FLI in Ewing's sarcoma. Mol Cancer Res 2006;4:851–9.
35. Lessnick SL, Dacwag CS, Golub TR. The Ewing's sarcoma oncoprotein EWS/FLI induces a p53-dependent growth arrest in primary human fibroblasts. Cancer Cell 2002;1:393–401.
36. May WA, Lessnick SL, Braun BS, Kiemsz M, Lewis BC, Lunsford LB, et al. The Ewing's sarcoma EWS/FLI-1 fusion gene encodes a more potent transcriptional activator and is a more powerful transforming gene than FLI-1. Mol Cell Biol 1993;13:7393–8.
37. Hollenhorst PC, Shah AA, Hopkins C, Graves BJ. Genome-wide analyses reveal properties of redundant and specific promoter occupancy within the ETS gene family. Genes Dev 2007;21:1882–94.
38. Gangwal K, Sankar S, Hollenhorst PC, Kinsey M, Haroldsen SC, Shah AA, et al. Microsatellites as EWS/FLI response elements in Ewing's sarcoma. Proc Natl Acad Sci USA 2008;105:10149–54.
39. Chaturvedi A, Hoffman LM, Welm AL, Lessnick SL, Beckerle MC, The EWS/FLI oncogene drives changes in cellular morphology, adhesion, and migration in Ewing sarcoma. Genes Cancer 2012;3:102–16.
40. Sankar S, Gomez NC, Bell R, Patel M, Davis IJ, Lessnick SL, et al. EWS and RE1-silencing transcription factor inhibit neuronal phenotype development and oncogenic transformation in Ewing sarcoma. Genes Cancer 2013;4:213–23.
41. Kauer M, Ban J, Kofler R, Walker B, Davis S, Meltzer P, et al. A molecular function map of Ewing's sarcoma. PLoS One 2009;4:e5415.
42. Tirado OM, Mateo-Lozano S, Villar J, Dettin LE, Llort A, Gallego S, et al. Caveolin-1 (CAV1) is a target of EWS/FLI-1 and a key determinant of the oncogenic phenotype and tumorigenicity of Ewing's sarcoma cells. Cancer Res 2006;66:9937–47.
43. Luo W, Gangwal K, Sankar S, Boucher KM, Thomas D, Lessnick SL. GSTM4 is a microsatellite-containing EWS/FLI target involved in Ewing's sarcoma oncogenesis and therapeutic resistance. Oncogene 2009;28:4126–32.
44. Dauphinot L, De Oliveira C, Melot T, Sevenet N, Thomas V, Weissman BE, et al. Analysis of the expression of cell cycle regulators in Ewing cell lines: EWS-FLI-1 modulates p57KIP2and c-Myc expression. Oncogene 2001;20:3258–65.
45. Prieur A, Tirode F, Cohen P, Delattre O, EWS/FLI-1 silencing and gene profiling of Ewing cells reveal downstream oncogenic pathways and a crucial role for repression of insulin-like growth factor binding protein 3. Mol Cell Biol 2004;24:7275–83.
46. Cironi L, Riggi N, Provero P, Wolf N, Suvà ML, Suvà D, et al. IGF1 is a common target gene of Ewing's sarcoma fusion proteins in mesenchymal progenitor cells. PLoS One 2008;3:e2634.
47. Li X, McGee-Lawrence ME, Decker M, Westendorf JJ. The Ewing's sarcoma fusion protein, EWS-FLI, binds Runx2 and blocks osteoblast differentiation. J Cell Biochem 2010;111:933–43.
48. Kang H-G, Jenabi JM, Zhang J, Keshelava N, Shimada H, May WA, et al. E-Cadherin cell-cell adhesion in Ewing tumor cells mediates suppression of anoikis through activation of the ErbB4 tyrosine kinase. Cancer Res 2007;67:3094–105.
49. May WA, Gishizky ML, Lessnick SL, Lunsford LB, Lewis BC, Delattre O, et al. Ewing sarcoma 11;22 translocation produces a chimeric transcription factor that requires the DNA-binding domain encoded by FLI1 for transformation. Proc Natl Acad Sci USA 1993;90:5752–6.
50. Bailly RA, Bosselut R, Zucman J, Cormier F, Delattre O, Roussel M, et al. DNA-binding and transcriptional activation properties of the EWS-FLI-1 fusion protein resulting from the t(11;22) translocation in Ewing sarcoma. Mol Cell Biol 1994;14:3230–41.
51. Zheng D, Zhao K, Mehler MF. Profiling RE1/REST-mediated histone modifications in the human genome. Genome Biol 2009;10:R9.
52. Sprüssel A, Schulte JH, Weber S, Necke M, Händschke K, Thor T, et al. Lysine-specific demethylase 1 restricts hematopoietic progenitor proliferation and is essential for terminal differentiation. Leukemia 2012;26:2039–51.
53. Stegmaier K, Wong JS, Ross KN, Chow KT, Peck D, Wright RD, et al. Signature-based small molecule screening identifies cytosine arabinoside as an EWS/FLI modulator in Ewing sarcoma. PLoS Med 2007;4:e122.
54. Mertz JA, Conery AR, Bryant BM, Sandy P, Balasubramanian S, Mele DA, et al. Targeting MYC dependence in cancer by inhibiting BET bromodomains. Proc Natl Acad Sci USA 2011;108:16669–74.
55. Delmore JE, Issa GC, Lemieux ME, Rahl PB, Shi J, Jacobs HM, et al. BET bromodomain inhibition as a therapeutic strategy to target c-Myc. Cell 2011;146:904–17.
56. Wang J, Lu F, Ren Q, Sun H, Xu Z, Lan R, et al. Novel histone demethylase LSD1 inhibitors selectively target cancer cells with pluripotent stem cell properties. Cancer Res 2011;71:7238–49.
57. Chau CM, Deng Z, Kang H, Lieberman PM. Cell cycle association of the retinoblastoma protein Rb and the histone demethylase LSD1 with the Epstein-Barr virus latency promoter Cp. J Virol 2008;82:3428–37.
58. Nair VD, Ge Y, Balasubramaniyan N, Kim J, Okawa Y, Chikina M, et al. Involvement of histone demethylase LSD1 in short-time-scale gene expression changes during cell cycle progression in embryonic stem cells. Mol Cell Biol 2012;32:4861–76.
59. Scoumanne A, Chen X, The lysine-specific demethylase 1 is required for cell proliferation in both p53-dependent and -independent manners. J Biol Chem 2007;282:15471–5.
60. Cho H-S, Suzuki T, Dohmae N, Hayami S, Unoki M, Yoshimatsu M, et al. Demethylation of RB regulator MYPT1 by histone demethylase LSD1 promotes cell cycle progression in cancer cells. Cancer Res 2011;71:655–60.
61. Huang J, Sengupta R, Espejo AB, Lee MG, Dorsey JA, Richter M, et al. p53 is regulated by the lysine demethylase LSD1. Nature 2007;449:105–8.
62. Nair SS, Li D-Q, Kumar R, A core chromatin remodeling factor instructs global chromatin signaling through multivalent reading of nucleosome codes. Mol Cell 2013;49:704–18.
63. McDonald OG, Wu H, Timp W, Doi A, Feinberg AP. Genome-scale epigenetic reprogramming during epithelial to mesenchymal transition. Nat Struct Mol Biol 2011;18:867–74.

Supplementary Materials

Supplementary Methods.

Table S1. Differentially Expressed Genes by RNA-seq – Supplementary Table S1.xls

Table S2. Nine-Gene Panel qRT-PCR Validation p-values – Supplementary Table S2.xls

Table S3. Primer Sequences

Figure S1. Transcriptional Profiling of HCI2509 in A673 and TTC-466

Figure S2. Morphological Changes in TTC-466 with HCI2509 Treatment

Figure S3. Effects of HCI2509 on Transformation, Methylation, and Apoptosis

Figure S4. Regulation of *HMOX1*

Figure S5. Tumor Volume, Body Weight, and Blood Counts

Supplementary Methods

RNA-seq data collection

RNA from A673 and TTC-466 cells treated with vehicle (0.3% DMSO) or 2 μM HCI2509 or stably infected and selected for expression of a control Luc-RNAi or the EF-2-RNAi or the EWS/ERG-RNAi was extracted using the RNAeasy kit (Qiagen) with an on-column DNAse digestion protocol. Libraries for deep-sequencing were prepared according to the manufacturer's instructions (Illumina) and sequenced on an Illumina Hi-Seq with 50 cycles of single end reads. Sequences from HCI2509 in A673, EWS/ERG knockdown, and HCI2509 in TTC-466 were aligned to the human genome build hg19. Raw sequence reads can be found in the NCBI SRA under numbers SRA096343, SRA096347, SRA096354, respectively. The USeq analysis package was used to identify differentially expressed genes (useq.sourceforge.net). Significance parameters were set to a 2-fold, 3-fold or 4-fold change in expression and an FDR of 0.1 (10%) or 1.0×10^{-10} or 1.0×10^{-15} as indicated in the figure legends.

Table S3. Primer Sequences for qRT-PCR analysis from RNA.

qRT-PCR primers:

Gene	Forward	Reverse
NKX2-2	5’ CTACGACAGCAGCGACAACC 3’	5’ GCCTTGGAGAAAAGCACTCG 3’
CAV1	5’ ATCGACCTGGTCAACCGCGAC 3’	5’ CGAAGTAAATGCCCCAGATGA 3’
E2F1	5’ GCCACTGACTCTGCCACCATA 3’	5’ GGTGGGGAAAGGCTGATGAAC 3’
IGF1	5’ GAAGATGCACACCATGTCCTC 3’	5’ CTCCAGCCTCCTTAGATCACA 3’
GSTM4	5’ GCTGCCCTACTTGATTGATGG 3’	5’TGATTGGAGACGTCCATAGCC 3’
HMOX1	5’ AACTTTCAGAAGGGCCAGGT 3’	5’ GTAGACAGGGGCGAAGACTG 3’
IGFBP3	5’ CATCAAGAAAGGGCATGCTAA 3’	5’ CTACGGCAGGGACCATATTCT 3’
CDH1	5’ TGCCCAGAAAATGAAAAAGG 3’	5’ GTGTATGTGGCAATGCGTTC 3’
RUNX2	5’ CCTCGGAGAGGTACCAGATG 3’	5’ AAACTCTTGCCTCGTCCACT 3’

Figure S1: Transcriptional Profiling of HCI2509 in A673 and TTC-466

A,B) Cell viability assay showing the difference in HCI2509 sensitivity between (A) TTC-466 cells with control and EWS/ERG knockdown or (B) NIH 3T3 cells with control and EWS/FLI expression. The dose-response curves were determined after 96 hours of treatment and normalized to the vehicle controls. n=3 for each point. Error bars denote standard deviation. EC_{50} and 95% CI were determined using GraphPad Prism 6. Note the line for ERG-RNAi data in (A) is a connecting line, not a curve fit.

C) Venn diagram representations of the overlap between the EWS/FLI and EWS/ERG transcription profiles, both generated by RNA-seq. Chi-square determined p-values are indicated with the observed contingency tables shown.

D) Gene set enrichment analysis (GSEA) using genes regulated by EWS/FLI in A673 cells (RNA-seq) as the rank-ordered dataset and the EWS/ERG-up-regulated or the EWS/ERG-down-regulated genesets (RNA-seq). Normalized enrichment scores (NES) and p-values are shown.

E,F) Venn diagram representations generated from respective RNA-seq data sets using default cutoffs (2-fold change, FDR=10%). (E) represents the overlap between the HCI2509 and the EWS/FLI-knockdown transcription profiles, both generated in A673 cells; (F) the overlap between the HCI2509 and the EWS/ERG-knockdown transcription profiles, both generated in TTC-466 cells. Chi-square determined p-values are indicated with the observed contingency tables shown.

G,H) GSEA using genes directly regulated by EWS/FLI in A673 cells (ChIP-chip and RNA-seq

overlap) as the geneset and HCI2509 regulated genes in A673 cells (RNA-seq) as the rank-ordered dataset in (G) or the vorinostat regulated genes in A673 cells (microarray) as the rank-ordered dataset in (H). Normalized enrichment scores (NES) and p-values are shown.

I,J) Top ten categories from DAVID functional analysis of the (I) EWS/FLI up-/HCI2509 down- and EWS/FLI down-/HCI2509 up-regulated genesets and (J) EWS/ERG up-/HCI2509 down- and EWS/ERG down-/HCI2509 up-regulated genesets. The log transformed enrichment scores for each category are indicated on the x-axis.

K) Validation of *NKX2.2*, *CAV1*, *GSTM4*, *E2F1*, *IGF-1*, *RUNX2*, *IGFBP3*, *HMOX1* and *CDH1* as HCI2509 targets by qRT-PCR analysis using EWS-502, SK-ES-1, SK-N-MC, and TC-71 cells treated for 48 hours with vehicle or HCI2509 at $2xEC_{50}$. The p-value for each fold-change is < 0.05 (n=3). Individual p-values are reported in Supplementary Table S2.

Figure S2: Morphological Changes in A673 and TTC466

A) Whole-field immunofluorescence images of A673 cells treated with increasing doses of HCI2509 for 72 hours. Staining was performed for F-actin stress fibers (red – phalloidin) and for focal adhesions (green –paxillin), and nuclei (blue). HCI2509 induced a dose-dependent increase in the cell spreading and morphology.

B,C) Immunofluorescence images of A673 cells treated with either control siRNA or LSD1 siRNA 50 nM for 48 hours. Staining was performed for (B) LSD1 and (C) F-actin stress fibers. Measurements of LSD1 nuclear signal and cell area were performed on at least 6 fields for each transfection. Decrease in LSD1 nuclear signal correlated with more organized actin fibers and cell spreading.

(D) Whole-field and (E) close-up immunofluorescence images of TTC-466 cells treated with increasing doses of HCI2509 for 3 days. Staining was performed for F-actin stress fibers (red – phalloidin) and for focal adhesions (green – paxillin), and nuclei (blue). HCI2509 induced a dose-dependent increase in the cell spreading and morphology.

F) Measurement of cell area in pixels in phalloidin images shows a dose-dependent increase in cell spreading with HCI2509. TTC-466 cells were fixed and stained with phalloidin. Cell area was quantified as previously described (*39)*.

Data is shown as scatter plot with mean plus standard deviation, and unpaired parametric t-test was used to determine p-values (* $p < 0.05$, *** $p < 0.0001$).

Figure S3: Effects of HCI2509 on Transformation, Methylation, and Apoptosis

A,B,C) Quantification of colonies formed by (A) EWS-502, (B) TC71, and (C) SK-ES-1 cells treated with either vehicle (0.3% DMSO) or varying doses of HCI2509. Error bars indicate SD of duplicate assays. EC_{50} values were determined using GraphPad Prism 6.

D) Representative western blot analysis of H3K4 and H3K9 methylation marks in A673 cells treated with either vehicle (0.3% DMSO) or 2 μM HCI2509 for 48 hours.

D,E,F) Cell viability and caspase activation at 0, 24, and 48 hours in (D) SK-N-MC, (E) TC71, and (F) SK-ES-1 cells treated with $2xEC_{50}$ HCI2509. Measurements were normalized to their respective vehicle (0.3% DMSO) sample at the appropriate time point. Error bars indicate SD (n=3).

Figure S4: Regulation of HMOX1

A) qRT-PCR for HMOX1 induction following treatment with candidate LSD1 inhibitors with respect to inhibitor biochemical potency against LSD1 in a biochemical assay (Cayman Chemical).

B) Western blot analysis to demonstrate expression of the RNAi-resistant 3x-FLAG tagged EWS/FLI, Δ22, or R2L2 cDNA constructs using an anti-FLAG antibody in A673 cells expressing a control shRNA (Luc) or an EWS/FLI shRNA. Tubulin was used as the loading control.

C) qRT-PCR analysis to assess level of knockdown of various co-repressors or *HMOX1* induction in A673 cells treated with either Luc-RNAi or RNAi for REST (REST p=3.53E-6, *HMOX1* p=1.92E-2), RCoR1 (RCoR1 p=1.18E-4, *HMOX1* p=3.67E-2), NCoR/SMRT (NCoR/SMRT p=2.60E-7, *HMOX1* p=5.85E-1), or Sin3A (Sin3A p=1.27E-6, *HMOX1* p=1.57E-1). Error bars indicate SD and p-values were determined using students t-test (n=3).

D) Western blot analysis for HMOX1 expression in A673 cells infected either with empty vector or an HA-tagged HMOX1 cDNA using an anti-HMOX1 antibody. Tubulin was used as a loading control.

E) Growth assays (3T5) for A673 cells described in (D). Student's t-test showed no significant difference in growth curves.

F) Quantification of colonies formed by A673 cells described in (D). Error bars indicate SD of duplicate assays.

Figure S5: Tumor Volume, Body Weight and Blood Counts

A) In vivo subcutaneous hind-flank xenograft studies measuring tumor volume for animals bearing tumors grown from (A) SK-ES-1 cells. The p-value was determined by 2-way ANOVA comparing the treatment curve to the vehicle curve. Individual tumor growth curves are shown for the vehicle-treated (blue) and HCI2509-treated (red) groups.

B,C,D) Body weight measurements for animals bearing tumors grown from (B) A673 cells, (C) SK-N-MC cells, and (D) SK-ES-1 cells. N=10 for all groups, with the exception of SK-N-MC HCI2509 treated group as noted. For body weights, the change in body weight normalized to day 0 was considered and a student's t-test was used to determine the p-value.

E) Blood counts for white blood cells (WBC), hematocrit (HCT), and platelets (PLT) from immunodeficient mice treated intraperitoneally either with vehicle or 40 mg/kg HCI2509 MWF for 24 days ± SD. Blood was drawn using a cheek draw and assayed at both day 0 and day 24. The normal range is reported.

Figure S1

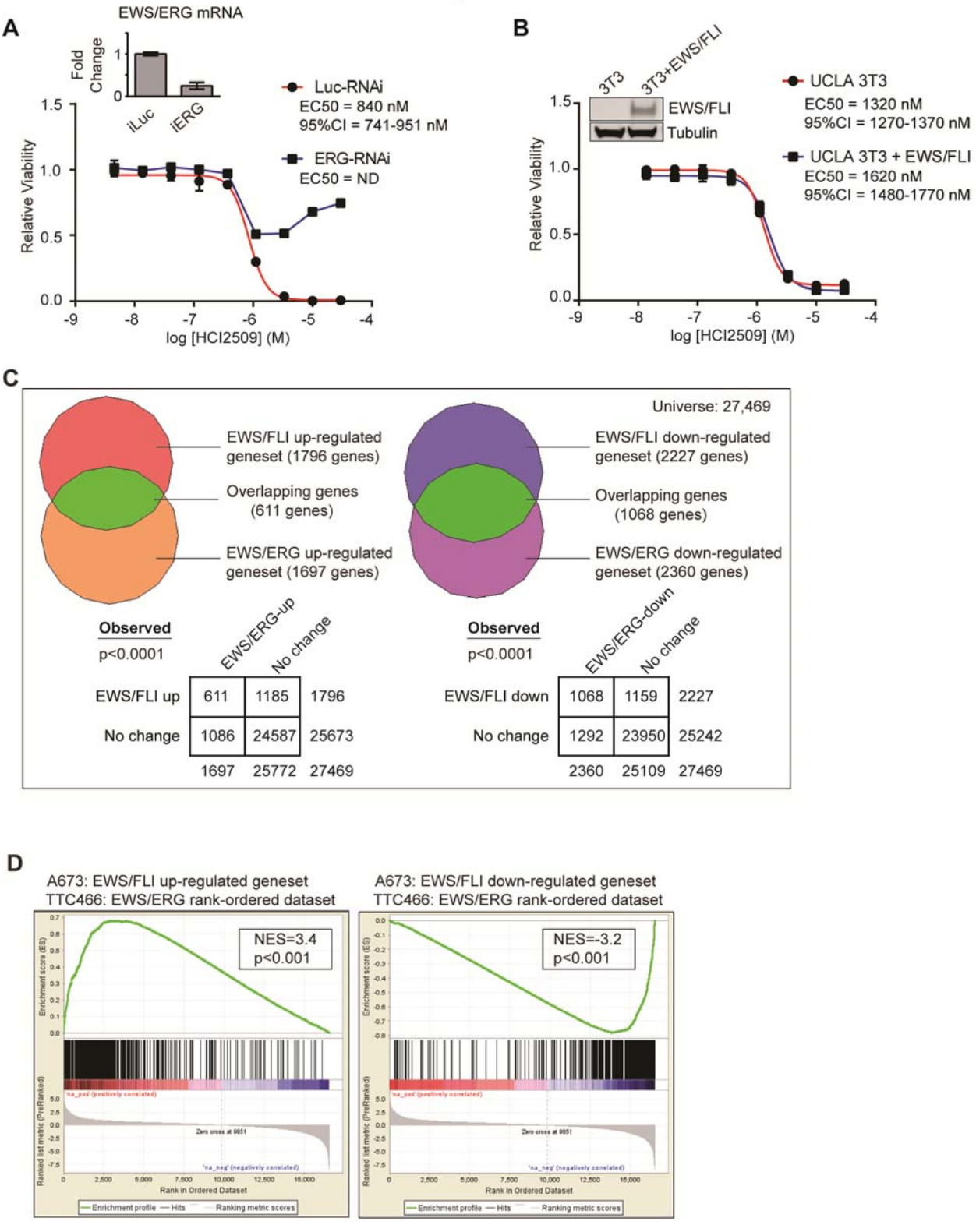
A
EWS/ERG mRNA
Fold Change
iLuc
iERG
Luc-RNAi
EC50 = 840 nM
95%CI = 741-951 nM
ERG-RNAi
EC50 = ND
Relative Viability
log [HCI2509] (M)
B
3T3
3T3+EWS/FLI
EWS/FLI
Tubulin
UCLA 3T3
EC50 = 1320 nM
95%CI = 1270-1370 nM
UCLA 3T3 + EWS/FLI
EC50 = 1620 nM
95%CI = 1480-1770 nM
C
Universe: 27,469
EWS/FLI up-regulated geneset (1796 genes)
Overlapping genes (611 genes)
EWS/ERG up-regulated geneset (1697 genes)
EWS/FLI down-regulated geneset (2227 genes)
Overlapping genes (1068 genes)
EWS/ERG down-regulated geneset (2360 genes)
Observed
p<0.0001
EWS/ERG-up
No change
EWS/FLI up 611 1185 1796
No change 1086 24587 25673
1697 25772 27469
Observed
p<0.0001
EWS/ERG-down
No change
EWS/FLI down 1068 1159 2227
No change 1292 23950 25242
2360 25109 27469
D
A673: EWS/FLI up-regulated geneset
TTC466: EWS/ERG rank-ordered dataset
NES=3.4
p<0.001
A673: EWS/FLI down-regulated geneset
TTC466: EWS/ERG rank-ordered dataset
NES=-3.2
p<0.001
Enrichment score (ES)
Ranked list metric (PreRanked)
Rank in Ordered Dataset
Enrichment profile
Hits
Ranking metric scores

Figure S1

E

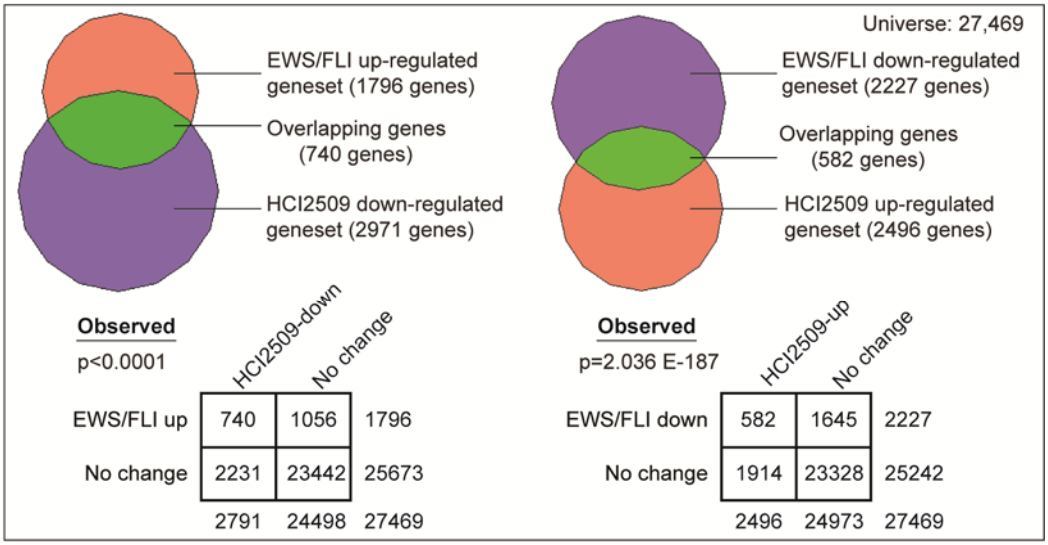

Observed p<0.0001

	HCI2509-down	No change	
EWS/FLI up	740	1056	1796
No change	2231	23442	25673
	2791	24498	27469

Observed p=2.036 E-187

	HCI2509-up	No change	
EWS/FLI down	582	1645	2227
No change	1914	23328	25242
	2496	24973	27469

F

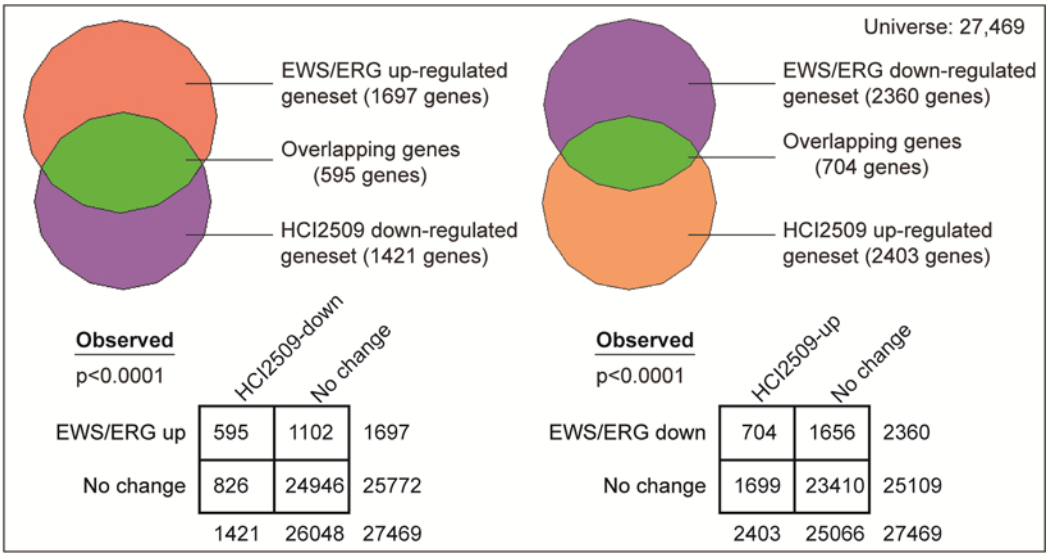

Observed p<0.0001

	HCI2509-down	No change	
EWS/ERG up	595	1102	1697
No change	826	24946	25772
	1421	26048	27469

Observed p<0.0001

	HCI2509-up	No change	
EWS/ERG down	704	1656	2360
No change	1699	23410	25109
	2403	25066	27469

G

A673: EWS/FLI direct up-regulated geneset
A673: HCI2509 rank-ordered dataset

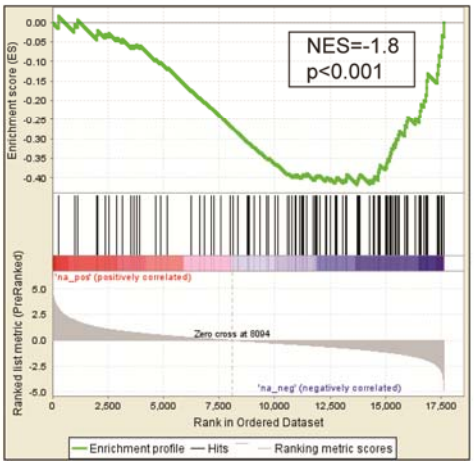

A673: EWS/FLI direct down-regulated geneset
A673: HCI2509 rank-ordered dataset

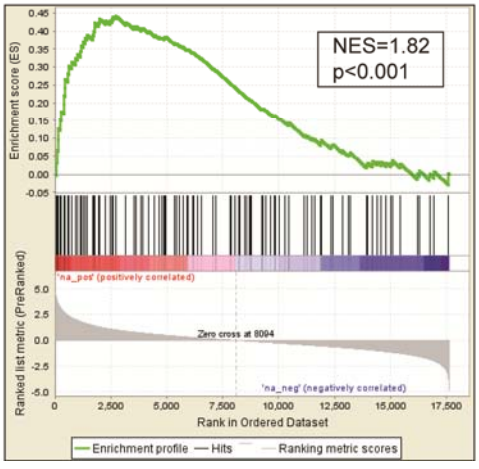

Figure S1

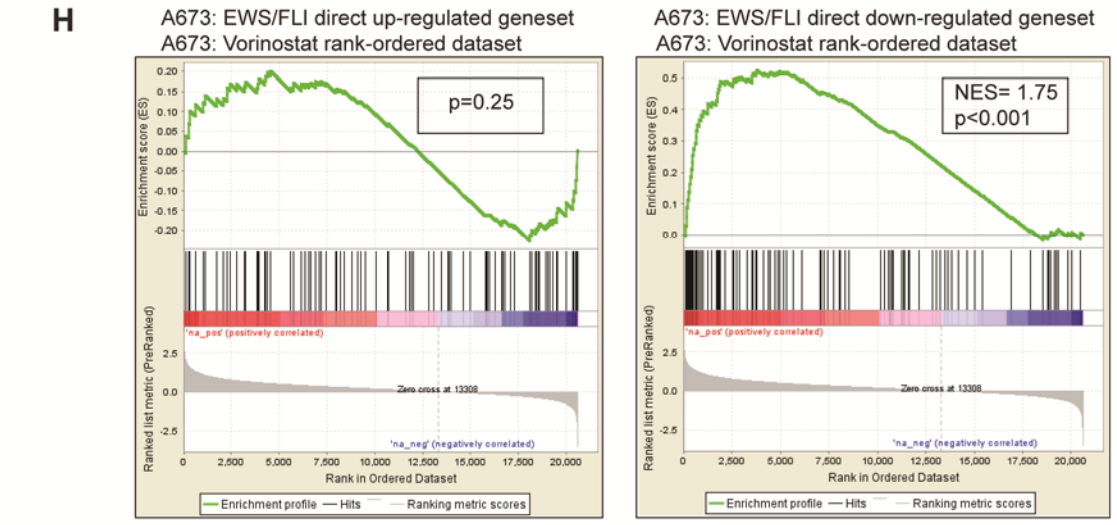
H
A673: EWS/FLI direct up-regulated geneset
A673: Vorinostat rank-ordered dataset
p=0.25
A673: EWS/FLI direct down-regulated geneset
A673: Vorinostat rank-ordered dataset
NES= 1.75
p<0.001
Enrichment score (ES)
Ranked list metric (PreRanked)
'na_pos' (positively correlated)
'na_neg' (negatively correlated)
Zero cross at 13308
Rank in Ordered Dataset
Enrichment profile
Hits
Ranking metric scores

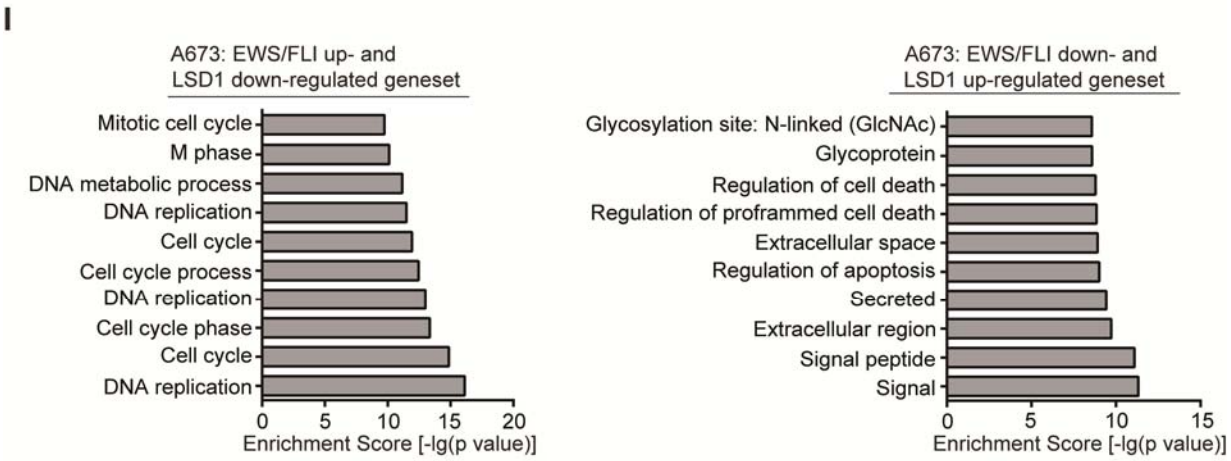
I
A673: EWS/FLI up- and
LSD1 down-regulated geneset
Mitotic cell cycle
M phase
DNA metabolic process
DNA replication
Cell cycle
Cell cycle process
DNA replication
Cell cycle phase
Cell cycle
DNA replication
Enrichment Score [-lg(p value)]
A673: EWS/FLI down- and
LSD1 up-regulated geneset
Glycosylation site: N-linked (GlcNAc)
Glycoprotein
Regulation of cell death
Regulation of proframmed cell death
Extracellular space
Regulation of apoptosis
Secreted
Extracellular region
Signal peptide
Signal
Enrichment Score [-lg(p value)]

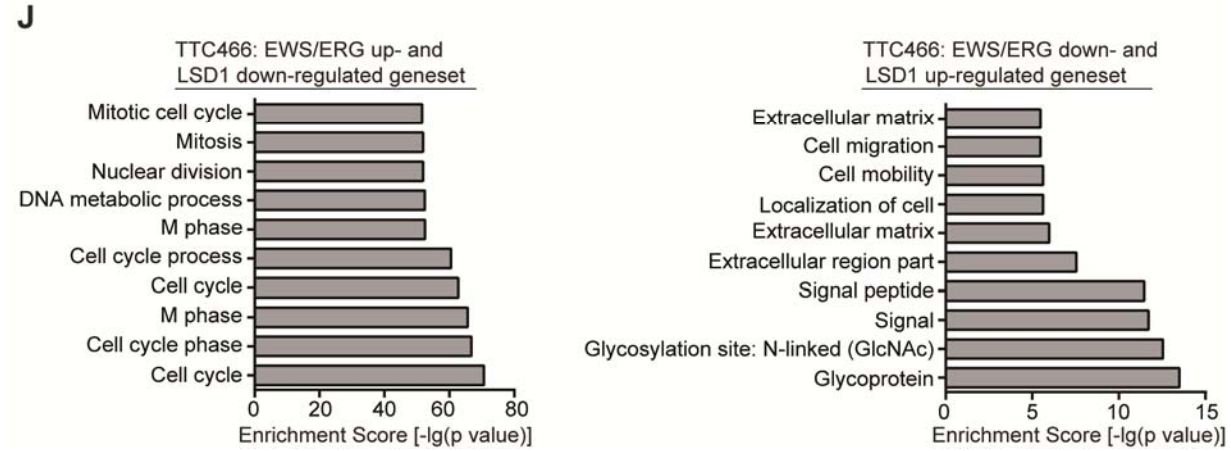
J
TTC466: EWS/ERG up- and
LSD1 down-regulated geneset
Mitotic cell cycle
Mitosis
Nuclear division
DNA metabolic process
M phase
Cell cycle process
Cell cycle
M phase
Cell cycle phase
Cell cycle
Enrichment Score [-lg(p value)]
TTC466: EWS/ERG down- and
LSD1 up-regulated geneset
Extracellular matrix
Cell migration
Cell mobility
Localization of cell
Extracellular matrix
Extracellular region part
Signal peptide
Signal
Glycosylation site: N-linked (GlcNAc)
Glycoprotein
Enrichment Score [-lg(p value)]

Figure S1

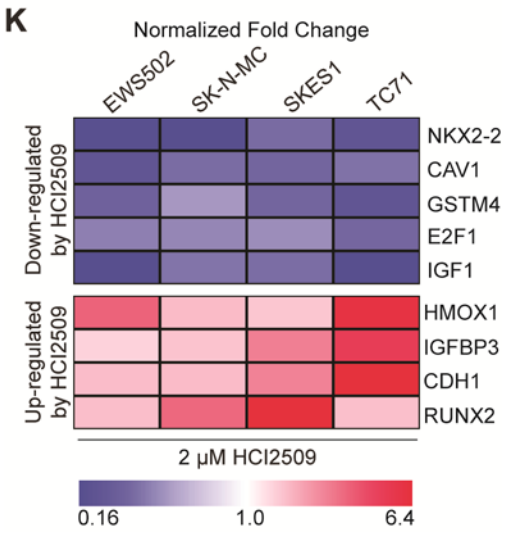
K
Normalized Fold Change
EWS502
SK-N-MC
SKES1
TC71
Down-regulated by HCI2509
NKX2-2
CAV1
GSTM4
E2F1
IGF1
Up-regulated by HCI2509
HMOX1
IGFBP3
CDH1
RUNX2
2 μM HCI2509
0.16
1.0
6.4

Figure S2

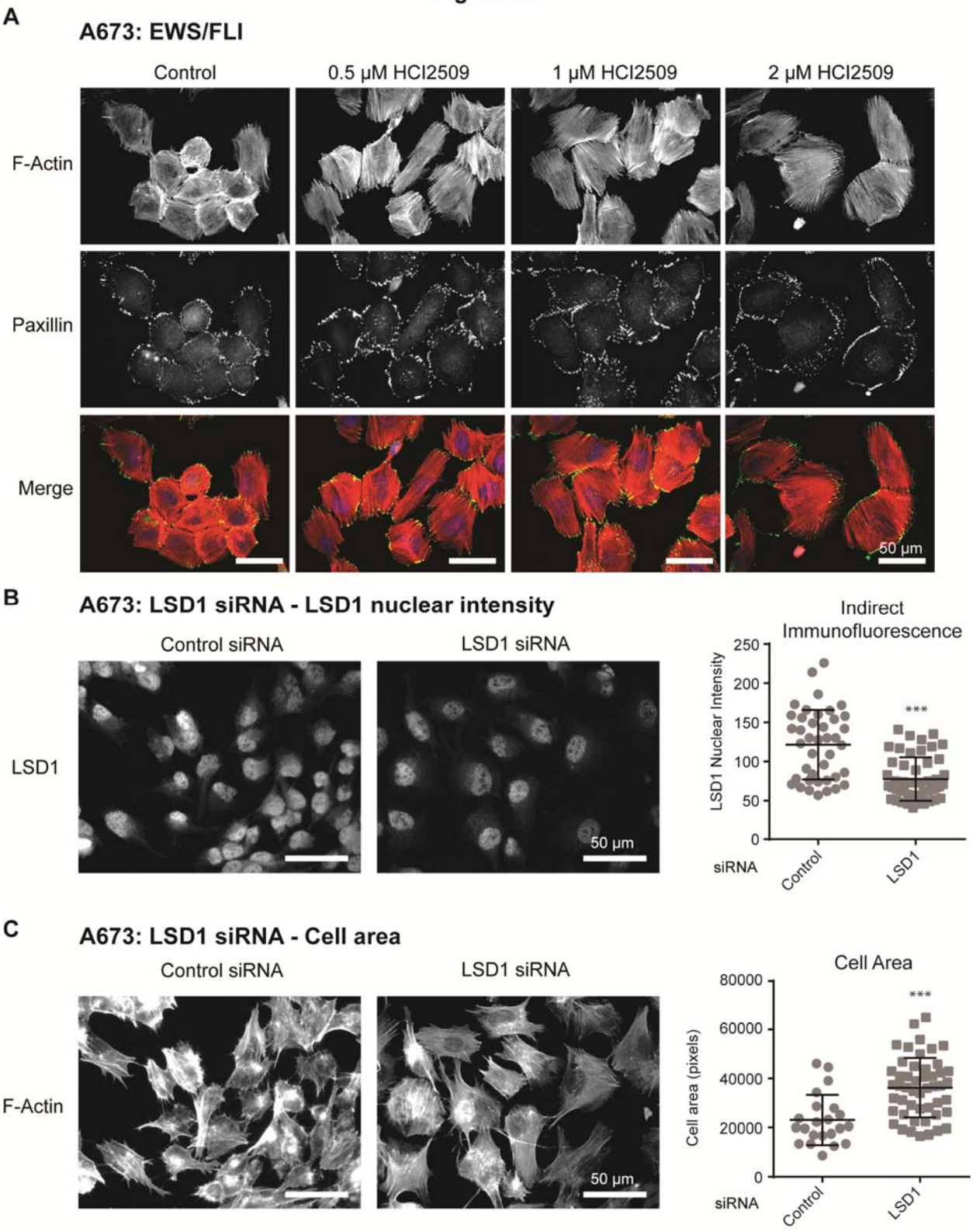
A
A673: EWS/FLI
Control
0.5 µM HCI2509
1 µM HCI2509
2 µM HCI2509
F-Actin
Paxillin
Merge
50 µm
B
A673: LSD1 siRNA - LSD1 nuclear intensity
Control siRNA
LSD1 siRNA
LSD1
50 µm
Indirect Immunofluorescence
LSD1 Nuclear Intensity
250
200
150
100
50
0
***
siRNA
Control
LSD1
C
A673: LSD1 siRNA - Cell area
Control siRNA
LSD1 siRNA
F-Actin
50 µm
Cell Area
Cell area (pixels)
80000
60000
40000
20000
0
***
siRNA
Control
LSD1

Figure S2

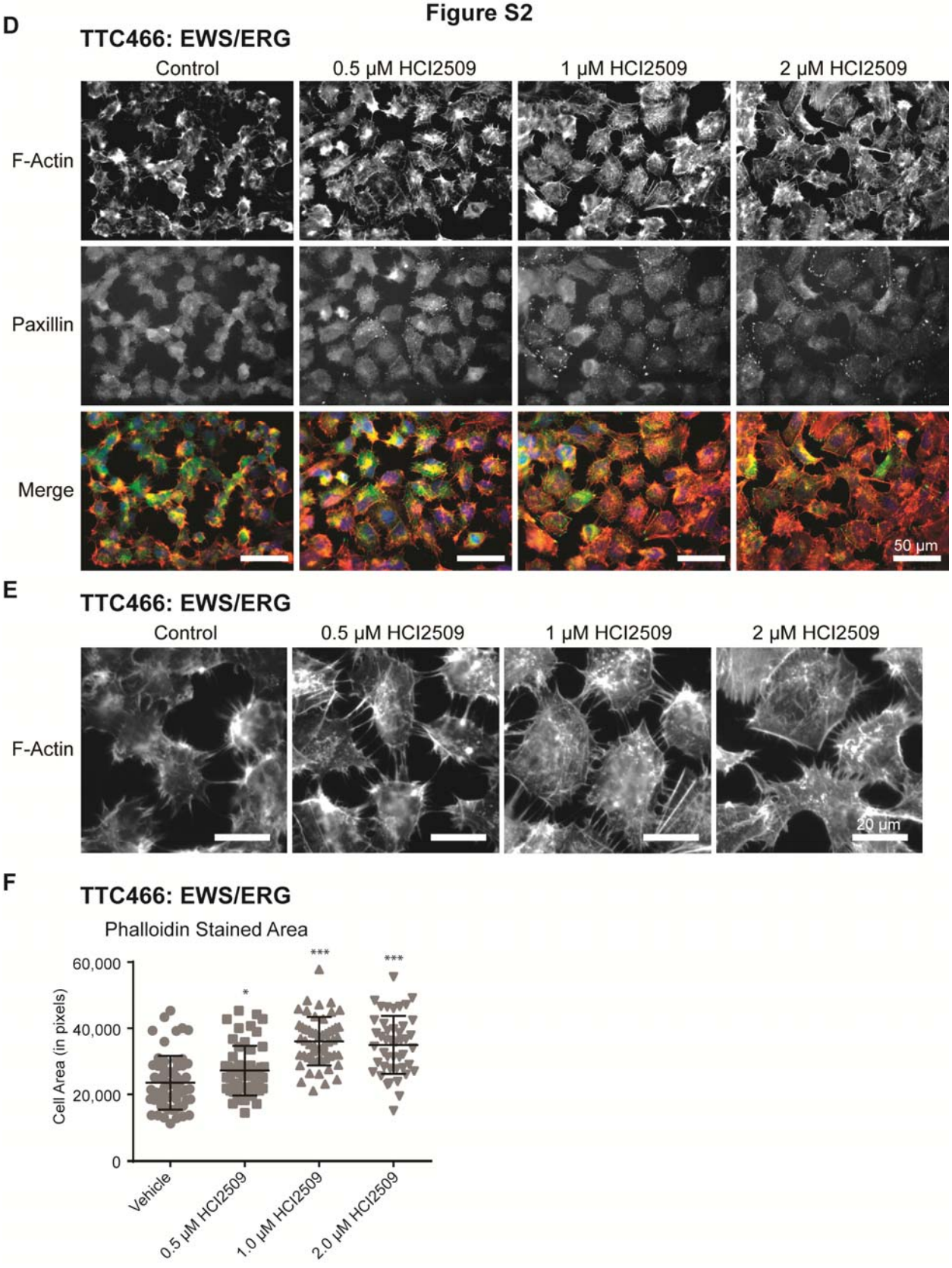
D
TTC466: EWS/ERG
Control
0.5 μM HCI2509
1 μM HCI2509
2 μM HCI2509
F-Actin
Paxillin
Merge
50 μm
E
TTC466: EWS/ERG
Control
0.5 μM HCI2509
1 μM HCI2509
2 μM HCI2509
F-Actin
20 μm
F
TTC466: EWS/ERG
Phalloidin Stained Area
Cell Area (in pixels)
60,000
40,000
20,000
0
*
***
***
Vehicle
0.5 μM HCI2509
1.0 μM HCI2509
2.0 μM HCI2509

Figure S3

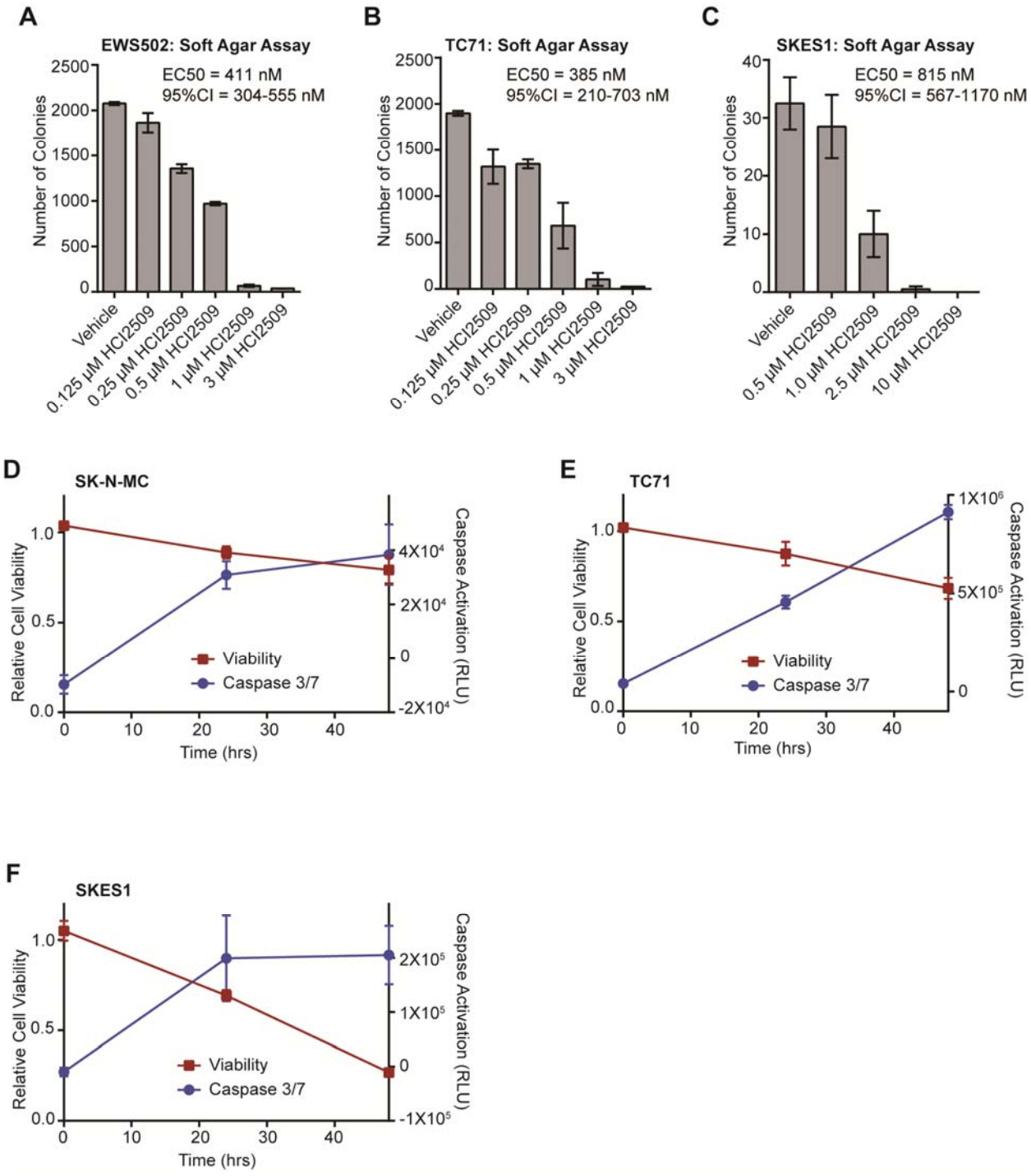
A
EWS502: Soft Agar Assay
EC50 = 411 nM
95%CI = 304-555 nM
Number of Colonies
2500
2000
1500
1000
500
0
Vehicle
0.125 μM HCl2509
0.25 μM HCl2509
0.5 μM HCl2509
1 μM HCl2509
3 μM HCl2509
B
TC71: Soft Agar Assay
EC50 = 385 nM
95%CI = 210-703 nM
Number of Colonies
2500
2000
1500
1000
500
0
Vehicle
0.125 μM HCl2509
0.25 μM HCl2509
0.5 μM HCl2509
1 μM HCl2509
3 μM HCl2509
C
SKES1: Soft Agar Assay
EC50 = 815 nM
95%CI = 567-1170 nM
Number of Colonies
40
30
20
10
0
Vehicle
0.5 μM HCl2509
1.0 μM HCl2509
2.5 μM HCl2509
10 μM HCl2509
D
SK-N-MC
Relative Cell Viability
1.0
0.5
0.0
Caspase Activation (RLU)
4X10⁴
2X10⁴
0
-2X10⁴
Viability
Caspase 3/7
0
10
20
30
40
Time (hrs)
E
TC71
Relative Cell Viability
1.0
0.5
0.0
Caspase Activation (RLU)
1X10⁶
5X10⁵
0
Viability
Caspase 3/7
0
10
20
30
40
Time (hrs)
F
SKES1
Relative Cell Viability
1.0
0.5
0.0
Caspase Activation (RLU)
2X10⁵
1X10⁵
0
-1X10⁵
Viability
Caspase 3/7
0
10
20
30
40
Time (hrs)

Figure S4

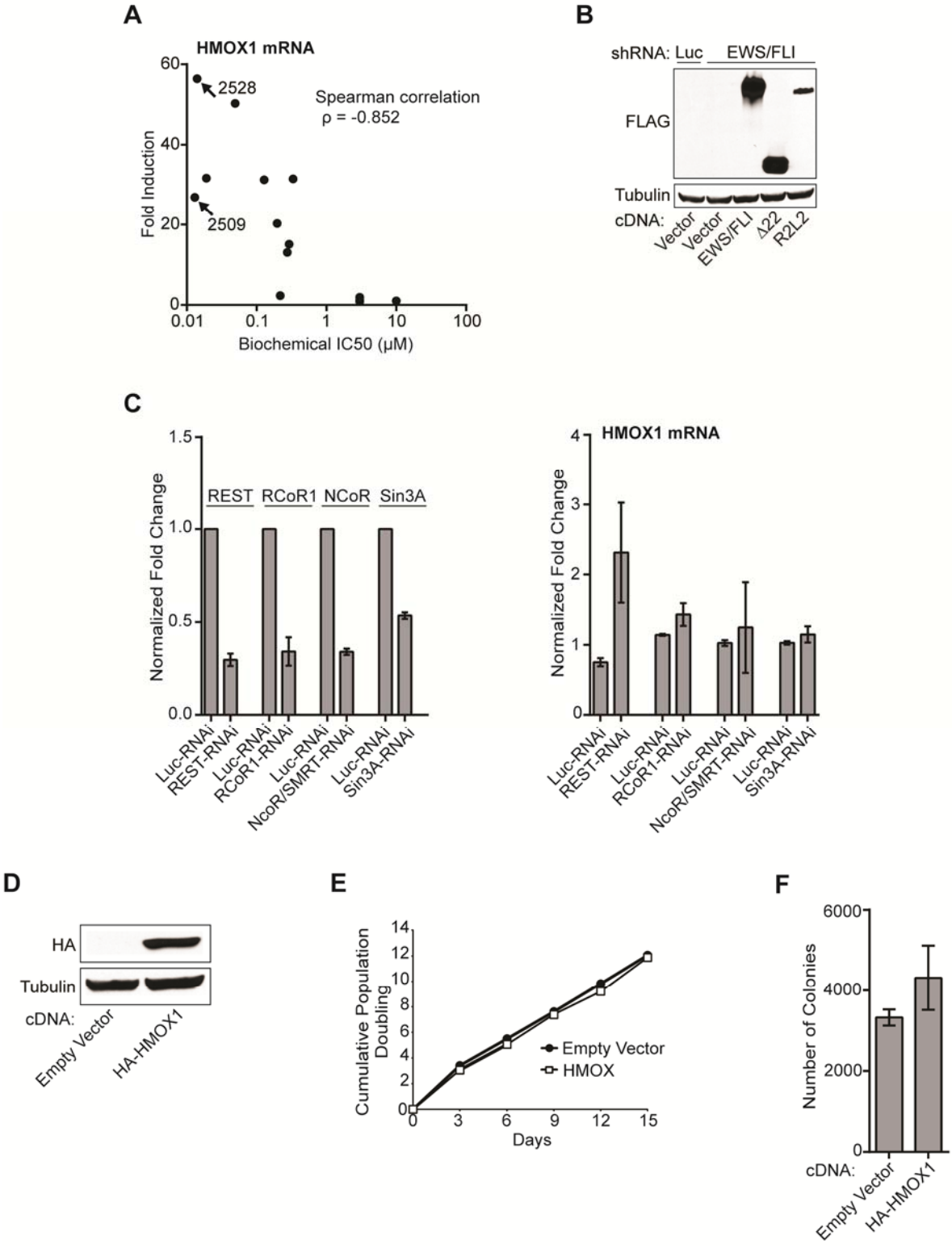
A
HMOX1 mRNA
2528
2509
Spearman correlation
ρ = -0.852
Fold Induction
Biochemical IC50 (μM)
B
shRNA: Luc
EWS/FLI
FLAG
Tubulin
cDNA:
Vector
Vector
EWS/FLI
Δ22
R2L2
C
REST
RCoR1
NCoR
Sin3A
Normalized Fold Change
Luc-RNAi
REST-RNAi
RCoR1-RNAi
NcoR/SMRT-RNAi
Sin3A-RNAi
HMOX1 mRNA
D
HA
Tubulin
cDNA:
Empty Vector
HA-HMOX1
E
Cumulative Population Doubling
Empty Vector
HMOX
Days
F
Number of Colonies
cDNA:
Empty Vector
HA-HMOX1

Figure S5

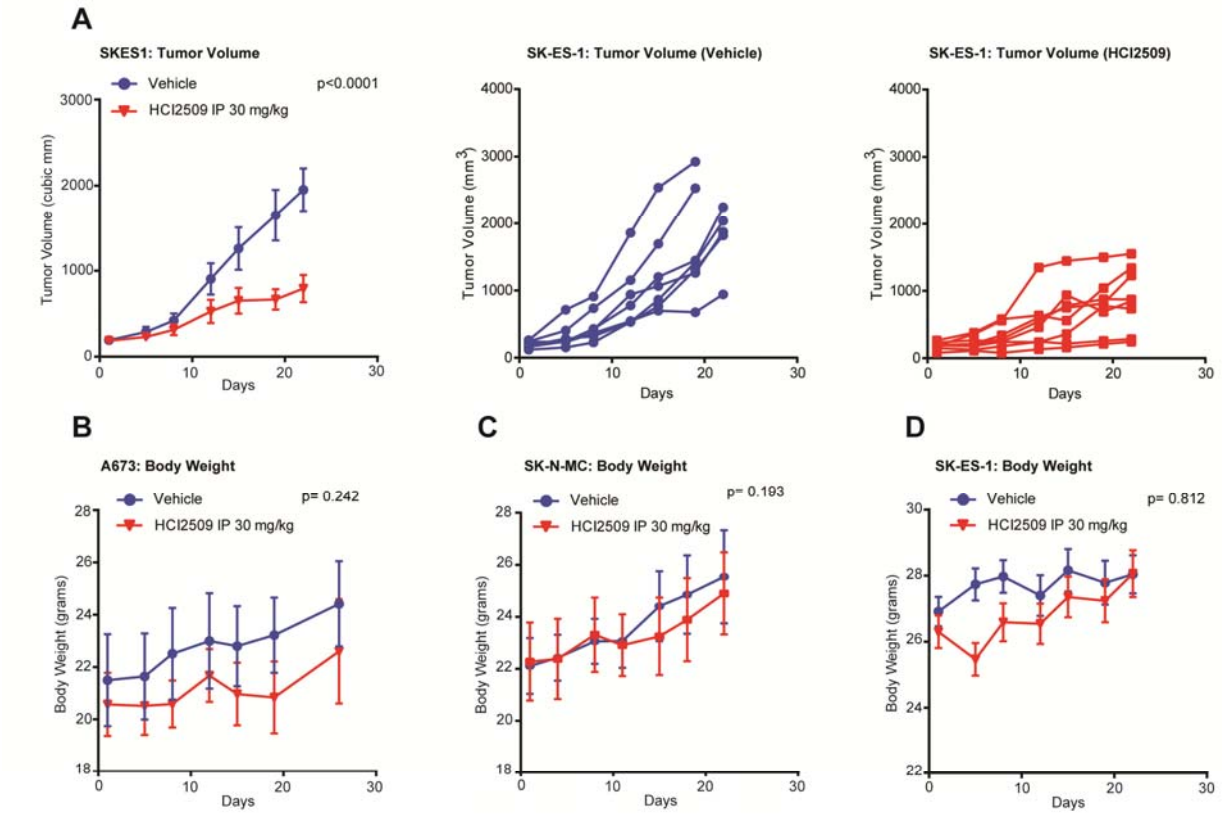

E

Measurement	Vehicle Day 0	Vehicle Day 24	2509 Day 0	2509 Day 24	Normal Range
WBC (x 10^3/μL)	6.53 ± 1.06	7.75 ± 4.13	9.15 ± 0.92	9.64 ± 3.25	2.6-10.1
HCT (%)	39.60 ± 6.76	42.75 ± 11.27	42.90 ± 12.44	44.20 ± 11.86	32.8-48.0
PLT (x 10^3/μL)	230.75 ± 55.09	214.00 ± 61.97	177.75 ± 45.02	195.00 ± 45.02	250-1540